Publications of the Astronomical Society of the Pacific, 138:104201 (26pp), 2026 October https://doi.org/10.1088/1538-3873/aea9cb
© 2026. The Author(s). Published by IOP Publishing Ltd on behalf of the Astronomical Society of the Pacific (ASP).

OPEN ACCESS

Honoring Paris Pişmiş' Legacy: Uniform Astrophysical Properties of 14 Understudied Clusters from Gaia DR3

Seliz Koç[1], Neslihan Alan[2], Furkan Akbaba[3], and Olcay Plevne[4]
[1] Department of Data Science and Analytics, Faculty of Engineering and Natural Sciences, Istanbul Galata University, 34440, Beyoğlu, Istanbul, Türkiye
[2] Fatih Sultan Mehmet Vakif University, Department of History of Science, 34664, Istanbul, Türkiye
[3] Institute of Graduate Studies in Science, Istanbul University, Istanbul, Türkiye
[4] Faculty of Science, Department of Astronomy and Space Sciences, Istanbul University, Istanbul, Türkiye; olcayplevne@istanbul.edu.tr
Received 2026 June 1; revised 2026 September 13; accepted 2026 September 18; published 2026 October 6

Abstract

Open clusters are fundamental tracers of the chemical and dynamical evolution of the Galactic disc. This study presents a systematic characterisation of 14 understudied open clusters from the Pismis catalog, selected as those for which the Gaia DR3 data support a well-defined stellar sequence, and spanning a wide range of ages and distances. Utilizing high-precision Gaia DR3 data, we aim to provide a high-fidelity modernisation of these historical discoveries while testing the consistency of our analytical framework across diverse stellar populations. Membership probabilities were determined via the unsupervised UPMASK algorithm using Gaia DR3 astrometric data (positions, proper motions, and parallax). To ensure high sample purity, the member samples entering the isochrone fits were restricted to $P \geqslant 0.90$, with all subsequent astrophysical parameters calculated through membership-weighted likelihoods. Fundamental properties-including age, distance, reddening, and metallicity-were derived using a Bayesian Nested Sampling approach to isochrone fitting, a methodology chosen for its robustness in navigating the parameter degeneracies typical of dense Galactic fields. The 14 systems exhibit a broad distribution of properties, with ages ranging approximately 11 Myr to 1.5 Gyr and distances spanning approximately 690 to 5445 pc. These refined and uniform parameters reconcile historical observations with the precision era of modern astrophysics, providing an internally homogeneous baseline for systems that large-scale automated surveys recover only partially. A direct cross-match against widely used automated catalogs shows that they typically contain only about a third of the members identified here, and substantially less in the most crowded fields, underscoring the value of cluster-specific analysis. This work contributes to a more complete census of the Galactic disc and sets out a reproducible, per-cluster reliability assessment that can be applied to the many comparable low-latitude systems that remain to be characterised.

Supplementary material for this article is available online

Unified Astronomy Thesaurus concepts: History of astronomy (1868); Interstellar medium wind (848); Open star clusters (1160); Bayesian statistics (1900)

1. Introduction

Open star clusters are widely used to study the structure and evolution of the Milky Way disk (e.g., Friel 1995; Dias et al. 2002; Cantat-Gaudin et al. 2020). Because the member stars within a single system form simultaneously from the collapse of the same giant molecular cloud, they share a common age, distance, and initial chemical composition (Lada & Lada 2003; Portegies Zwart et al. 2010; Kim et al. 2017). This physical homogeneity reduces the number of free parameters, making open clusters as a whole—not merely the main-sequence morphology of an individual system—reliable benchmarks for testing stellar evolution models. Located close to the Galactic plane, their spatial distribution provides a direct way to trace the large-scale layout of the Galactic disk (Friel 1995; Cantat-Gaudin et al. 2020; Castro-Ginard et al. 2022). They are, in effect, the only population that simultaneously carries a reliable age, a reliable distance, and a reliable composition, which is why they remain the primary calibrators of the disc age–metallicity relation, of the radial abundance gradient and its evolution, and of cluster dissolution timescales (Krumholz et al. 2019; Netopil et al. 2022; Spina et al. 2022; Akbaba et al. 2024; Horta et al. 2026).

Original content from this work may be used under the terms of the Creative Commons Attribution 4.0 licence. Any further distribution of this work must maintain attribution to the author(s) and the title of the work, journal citation and DOI.

The systematic study of these systems is old enough to have passed through several distinct observational regimes. The visual era, culminating in the survey of the southern sky by Herschel & Frederick William (1847), established which condensations existed but said little about what they were. Physical characterisation began with photographic photometry: Trumpler (1930) used it to place clusters on a common distance scale, to introduce the concentration classes still in use, and—through the systematic reddening of distant clusters—to establish interstellar absorption itself. The following decades were dominated by wide-field photographic surveys of the southern Milky Way, which is where most previously uncataloged clusters were still hiding; the classification schemes and compilations that organised these discoveries (e.g., Ruprecht 1966) defined the working census of open clusters for the rest of the century.

The Pismis catalog has an established place among these surveys. It is named after Marie Paris Pişmiş (1911–1999),[5] who, analyzing wide-field photographic plates obtained with the Schmidt camera of the Tonantzintla Observatory, Mexico, identified 24 open clusters and two globular clusters, introducing the Pismis catalog to the literature (Pişmiş 1959). The search was deliberately directed at low Galactic latitudes, towards the inner disc and the third quadrant, precisely where crowding and extinction had kept earlier surveys from being complete. That choice is the reason the catalog exists, and, as shown below, it is also the reason its members have remained difficult objects ever since.

The observational regime changed again with the arrival of all-sky astrometry. The Gaia space mission (Gaia Collaboration et al. 2016), particularly Data Release 3 (DR3; Gaia Collaboration et al. 2023), significantly increased the astrometric and photometric precision available for stellar cluster analysis. Parallaxes and proper motions of individual stars turned membership determination from a photometric plausibility argument into a measurement, and unsupervised clustering applied to the resulting astrometric space has both revised the membership of classical clusters and expanded the census by thousands of new candidates (Cantat-Gaudin et al. 2018; Castro-Ginard et al. 2022; Hunt & Reffert 2023, 2024). Homogeneous parameter catalogs built on these membership lists (e.g., Bossini et al. 2019; Cantat-Gaudin et al. 2020; Dias et al. 2021) now cover the disc well enough to trace spiral structure and the warp (Joshi et al. 2016; Poggio et al. 2021), while the large spectroscopic surveys—Gaia-ESO, OCCAM/APOGEE, and their successors—have added chemical abundances for hundreds of clusters and, with them, a far sharper picture of the radial metallicity gradient (Donor et al. 2020; Netopil et al. 2022; Randich et al. 2022; Spina et al. 2022). The scale of the census has in turn made automated parameter estimation a necessity, and pipelines that fit thousands of clusters in a single pass—whether by neural networks trained on synthetic populations (Cavallo et al. 2024) or by Bayesian nested sampling applied cluster by cluster (Akbaba et al. 2026; Plevne & Akbaba 2026)—now supply ages, distances and extinctions for the bulk of the known population. Taken together, these programmes have made the open-cluster population a statistically usable tracer of the disc for the first time.

The strength of these surveys, however, is statistical, and it is bought at a price that is paid unevenly across the sky. While global automated surveys catalog thousands of open clusters, their effectiveness decreases for heavily reddened targets, sparse systems, or dense fields toward the inner Galactic disk, a limitation we quantify directly for the present sample in Section 4.2. Different automated pipelines (e.g., Dias et al. 2002; Kharchenko et al. 2013; Sampedro et al. 2017; Cantat-Gaudin et al. 2020; Hunt & Reffert 2023) therefore often yield discrepant fundamental parameters for the same clusters. These variations arise from different membership selection criteria, the handling of faint stars, and the inherent age–distance–reddening degeneracy, the latter of which we discuss concretely for a subset of the present sample in Section 5.2. A uniform pipeline must adopt uniform thresholds—on field density, on the number of recovered members, on the tolerated contamination—and objects that sit near those thresholds are either assigned truncated membership lists or dropped altogether. Because the thresholds are set by what works for the bulk of the population, the systems that fail them are not a random subset: they are concentrated at low $|b|$, at high extinction, and towards the inner disc. Cluster-specific analysis is required to resolve these discrepancies, and it is exactly in this regime that it is still required.

The Pismis clusters fall squarely in that regime, and this is what makes them worth revisiting now. Despite their historical importance, a significant portion of the Pismis open clusters has lacked homogeneous investigation. While specific objects have been analyzed through dedicated multi-wavelength studies (e.g., Carraro & Seleznev 2012; Hatzidimitriou et al. 2019; Baravalle et al. 2021), many systems still lack a consistent characterization based on high-precision data. They are understudied not by accident but by circumstance: all 14 of the targets analyzed here lie within $|b| \leqslant 3.^{\circ}21$ of the Galactic plane and thirteen suffer moderate-to-high extinction ($A_V > 1$ mag, reaching 3.7 mag for Pismis 3), placing the sample in precisely the crowded, heavily reddened inner and third-quadrant disc where automated catalogs are least reliable. This coincidence turns a tribute into a controlled experiment. Rather than adding one more parameter catalog—a task already addressed by wide-field surveys—we use these difficult systems to ask a specific, quantitative question: in

[5] One of the earliest prominent female astronomers globally, Pişmiş was the first woman to earn a Ph.D. in mathematics from Istanbul University, Türkiye. She pioneered astronomy research in Türkiye and subsequently made pivotal contributions to shaping the infrastructure of modern Mexican astrophysics.

the crowded, reddened disc, how much does cluster-specific membership analysis change the recovered stellar population relative to automated pipelines, how does that difference propagate into the inferred astrophysical parameters, and which of those parameters can be trusted?

To honor the memory and scientific legacy of Paris Pişmiş, this study provides a uniform re-evaluation of a sample of 14 Pismis open clusters selected as suitable for analysis (the selection criteria and the full list of targets are given in Section 2.3). Our analysis relies on a Bayesian Nested Sampling isochrone fitting approach to derive the fundamental astrophysical parameters of these selected clusters. To constrain this Bayesian framework, we first establish cluster membership from the Gaia DR3 database using the unsupervised UPMASK algorithm (Krone-Martins & Moitinho 2014). This methodology is widely used both in wide-field surveys and in dedicated single-cluster analyses to isolate cluster members from field star contamination (e.g., Cantat-Gaudin et al. 2020; Castro-Ginard et al. 2020; Koc & Yontan 2023; Ahmed & Tadross 2025; Yontan et al. 2026), including recent studies that combine it with ground-based photometry to characterise individual systems in detail (Çakmak et al. 2024; Karagöz et al. 2025; Tanık Öztürk et al. 2025). Processing the entire sample through this single pipeline yields an internally homogeneous set of parameters, free of the study-to-study methodological scatter that affects heterogeneous literature compilations, and thus a uniform baseline for comparing these systems within the Galactic disc; we quantify in Section 4.2 how far the resulting membership samples and parameters depart from those of the automated catalogs.

We then confront these membership-weighted results, cluster by cluster, both with the major automated catalogs (Section 4.2) and with a quantitative fit-reliability framework of our own (Section 5.2). The intended contribution is therefore twofold. First, homogeneous and reproducible fundamental parameters for 14 systems that the modern census has largely passed over, closing a gap left open since the plates were taken. Second, and more generally, a direct measurement of how much automated membership assignment costs in the reddened inner disc, together with an explicit, per-cluster statement of which derived parameters survive that regime and which do not—a diagnostic that is transferable to the many other low-latitude clusters awaiting the same treatment.

The remainder of this paper is structured as follows. Section 2 describes the Gaia data retrieval and quality filters (Section 2.1), the literature context for the selected clusters (Section 2.2), and the reduction of the original catalog from 24 to the 14 analyzable systems (Section 2.3). Section 3 presents the method: membership determination with UPMASK and the resulting astrometric parameters (Section 3.1), followed by the Bayesian Nested Sampling isochrone fitting used to derive ages, distances, reddenings, and metallicities (Section 3.2). Section 4 reports the derived parameters, using Pismis 18 as a worked example of the posterior diagnostics, and compares both our membership samples and our parameters against the major automated catalogs (Section 4.2). Section 5 discusses the results: cluster-by-cluster notes against prior studies, the fit-reliability framework that identifies which parameters can be trusted (Section 5.2), the sample in the context of the Galactic disc, and the current state of its spectroscopic coverage (Section 5.5). The main conclusions are summarised in Section 6. Supporting posterior and CMD diagnostics for the full sample are provided as online supplementary material, and the complete parameter table is collected in Appendix.

2. Data

2.1. Gaia Data Retrieval and Quality Filters

Data for the Pismis open clusters were retrieved from the Gaia Archive using Data Release 3 (DR3; Gaia Collaboration et al. 2023). For each of the 24 clusters in the original catalog of Pişmiş (1959), we performed a spatial cone search centred on the literature coordinates listed in Table 2, using a radius of 40 arcminutes (40′). This search radius sufficiently covers the cluster area while providing an adequate field-star population for the membership assignment described in Section 3.1. The retrieved data set comprises five-parameter astrometric solutions—celestial coordinates (α, δ), proper motions ($\mu_\alpha \cos\delta$, μ_δ), and parallax (ϖ)—together with G, $G_{\rm BP}$, and $G_{\rm RP}$ photometry.

To ensure high astrometric quality, sources were filtered using a Renormalised Unit Weight Error threshold of RUWE < 1.4 (Lindegren et al. 2018), and only stars with a relative parallax uncertainty $\sigma_\varpi/\varpi \leqslant 0.2$ were retained. Because RUWE increases sharply for astrometric solutions perturbed by an unresolved companion, this cut simultaneously removes a fraction of the unresolved binary population from the sample (Lindegren et al. 2021). While this improves the purity of the single-star sequence used for isochrone fitting, it implies that the resulting membership catalogs are not suited to inferring the intrinsic binary fraction of these clusters, and that our sample is biased against short-period binaries with the most strongly perturbed astrometric solutions.

Photometric analysis and evolutionary modelling were performed using G versus ($G_{\rm BP} - G_{\rm RP}$) colour–magnitude diagrams (CMDs). To restrict photometric errors to acceptable limits—typically below 0.01 mag in G and 0.1 mag in the colour index—and to mitigate incompleteness at the faint end of the Gaia survey, a magnitude limit of $G < 19$ mag was applied across the sample; this restricts the analysis to the magnitude range in which Gaia DR3 astrometric and photometric solutions are most reliable in uncrowded fields. Because parallax precision degrades toward fainter magnitudes, this cut acts jointly with the $\sigma_\varpi/\varpi \leqslant 0.2$ criterion to preferentially retain upper-main-sequence and turn-off stars,

which dominate the age-sensitive part of the CMD, at the expense of the faintest, most distant candidate members.

In practice, however, the magnitude limit is not what truncates the sample. Applied to the 52,103 sources that pass the remaining quality criteria across the 14 fields, 41.4% have $G \geqslant 19$, but 99.8% of those are already removed by the relative parallax criterion $\sigma_{\varpi}/\varpi \leqslant 0.2$; the magnitude cut alone eliminates 36 sources, or 0.07% of the field sample. The same holds for the members: of the 3464 high-probability members (Section 3.1) that satisfy every other criterion, only 17 are excluded by $G < 19$ and not already by the parallax criterion, against 805 excluded by the parallax criterion alone. The faint limit of our member catalogs is therefore set by the precision of the Gaia astrometry, not by the adopted magnitude cut, and the two are not independent choices: parallax uncertainty grows steeply toward faint magnitudes, so a 20% relative-parallax criterion already implies a magnitude limit of its own. Consistently with this, the faintest retained member lies below $G = 19$ in all 14 clusters, ranging from $G = 17.2$ for Pismis 1 to $G = 19.0$ for Pismis 6.

For the more distant systems the limit is additionally imposed by distance itself, independent of the adopted magnitude cut. At the reddening and distance we derive for Pismis 7 ($d = 5367$ pc, $A_G = 2.03$ mag), $G = 19$ corresponds to an absolute magnitude of $M_G \approx 3.3$, that is, to the immediate vicinity of the main-sequence turn-off; the same limit corresponds to $M_G \approx 9.3$ for the nearest cluster, Pismis 4 at 690 pc. In the distant, reddened clusters the entire observable sequence therefore lies above the magnitude limit, and the low-mass main sequence is inaccessible regardless of where the cut is placed. This is the sense in which our member samples are complete: they contain the age-sensitive part of the CMD in full, and are truncated below it by the depth of the survey rather than by the adopted selection criteria. To maintain physical consistency with the PARSEC stellar evolution models (Bressan et al. 2012) used for isochrone fitting (Section 3.2), we adopted the photometric zero-point corrections and passband definitions of Riello et al. (2021). This data preparation enables the reliable determination of fundamental parameters, including age, distance, and reddening, through the Bayesian Nested Sampling approach (Skilling 2004) described in Section 3.2.

2.2. *Literature Context for the Selected Clusters*

The literature record for the 14 selected Pismis clusters is markedly uneven, ranging from systems with essentially no dedicated study to a handful with multiple independent age and distance determinations. Table 1 compiles the fundamental parameters reported by four representative wide-field Gaia-based catalogs (Kharchenko et al. 2013; Cantat-Gaudin et al. 2020; Dias et al. 2021; Hunt & Reffert 2024).

Several clusters lack any dedicated individual investigation and are characterised solely through automated survey pipelines: Pismis 4 (Table 1; Cantat-Gaudin et al. 2020; Dias et al. 2021; Hunt & Reffert 2024), and Pismis 14, for which the values reported by Bukowiecki et al. (2011) and Kharchenko et al. (2013) show significant discrepancies stemming from the inherent limitations of automated catalog data (Carraro et al. 2017). Pismis 1, despite inclusion in global surveys (Cantat-Gaudin et al. 2020; Hunt & Reffert 2024), remains poorly constrained owing to its proximity to the Galactic plane and severe line-of-sight contamination (Pişmiş 1959).

For several other systems, dedicated photometric studies exist but disagree substantially on age, distance, or metallicity. Pismis 3 spans age estimates from ∼1.1 to ∼3 Gyr and distances from 1.5 to 2.8 kpc across independent analyses (Carraro & Ortolani 1994; Tadross 2008; Bisht et al. 2022; Obasi et al. 2025; Zhang et al. 2025). Pismis 7, 13, and 19 show comparable levels of disagreement between early photometric work (Vogt & Moffat 1973; Claria 1979; Phelps et al. 1994; Piatti et al. 1998; Ahumada 2005) and more recent Gaia-based or CCD studies (Carraro & Munari 2004; Giorgi et al. 2005; Cantat-Gaudin et al. 2020; Çakmak et al. 2021; Poggio et al. 2021; Bisht et al. 2022). Pismis 15 and Pismis 18, the two most extensively studied clusters in the sample, have converging age estimates near 0.7–1.4 Gyr (Piatti et al. 1998; Carraro et al. 2005; Tadross 2008; Hatzidimitriou et al. 2019; Peña Ramírez et al. 2021; Bisht et al. 2022; Belwal et al. 2025), though their metallicity determinations remain in tension (see Section 5.1).

Two clusters, Pismis 6 and Pismis 8, have been proposed as a physically associated binary system sharing a common age of order 1–10 Myr (Kopchev et al. 2008), based on early classifications as young clusters (Vogt & Moffat 1973; FitzGerald et al. 1979; Forbes & Short 1994; Giorgi et al. 2005); this putative association remains unconfirmed. Pismis 9, in contrast, has recently been established as an independent foreground cluster unrelated to the nearby NGC 2659 (Giorgi et al. 2023; Gregorio-Hetem & Hetem 2024), and Pismis 5 has been linked to a primordial triple-cluster system within the Vela Molecular Cloud (Vogt & Moffat 1973; Bonatto & Bica 2009; Dias et al. 2021; Qin et al. 2023). Pismis 12, finally, shows unusually consistent literature parameters across near-infrared and Gaia-based studies alike (Bica & Bonatto 2011; Bisht et al. 2022).

This heterogeneity in observational coverage and methodology—spanning photographic, 2MASS, and multiple Gaia data releases—motivates the uniform, membership-weighted reanalysis presented in this work. A detailed cluster-by-cluster comparison between our results and this literature record is given in Section 5.1.

Table 1
Literature Compilation of Fundamental Parameters for Selected Pismis Clusters

Cluster	log(Age)	Distance (pc)	[Fe/H] (dex)	A_V (mag)
Pismis 1	7.800 (1), 7.470 (2), 7.031 (3), 8.180 (4)	5903 (1), 5666 (2), 4333 (3), 4630 (4)	−0.194 (3)	1.807 (1), 1.690 (2), 2.044 (3)
Pismis 3	8.925 (1), 9.500 (2), 8.996 (3), 9.026 (4)	1418 (1), 2349 (2), 2064 (3), 2112 (4)	−0.076 (3)	3.680 (1), 2.350 (2), 3.313 (3)
Pismis 4	8.155 (1), 8.080 (2), 8.094 (3), 8.066 (4)	575 (1), 695 (2), 691 (3), 681 (4)	−0.200 (1), −0.089 (3)	0.031 (1), 0.180 (2), 0.292 (3)
Pismis 5	7.300 (1), 7.000 (2), 6.883 (3), 6.637 (4)	702 (1), 941 (2), 921 (3), 913 (4)	−0.034 (3)	2.582 (1), 1.480 (2), 1.388 (3)
Pismis 6	7.580 (1), 7.410 (2), 7.285 (3), 7.600 (4)	1668 (1), 1763 (2), 1737 (3), 1720 (4)	0.126 (3)	1.181 (1), 1.000 (2), 1.401 (3)
Pismis 7	8.705 (1), 8.890 (2), 8.968 (3), 8.487 (4)	4783 (1), 4611 (2), 3843 (3), 4947 (4)	−0.225 (3)	2.905 (1), 1.600 (2), 2.078 (3)
Pismis 8	7.430 (1), 7.510 (2), 7.137 (3), 7.675 (4)	1363 (1), 1903 (2), 1756 (3), 1765 (4)	−0.034 (3)	2.195 (1), 1.580 (2), 2.077 (3)
Pismis 9	7.360 (1), 8.500 (2), 7.608 (3), 8.458 (4)	1713 (1), 2120 (2), 1815 (3), 1865 (4)	−0.080 (3)	1.581 (1), 1.590 (2), 1.528 (3)
Pismis 12	9.205 (1), 9.090 (2), 9.087 (3), 9.101 (4)	2221 (1), 2107 (2), 2114 (3), 2094 (4)	−0.146 (3)	1.615 (1), 1.410 (2), 1.999 (3)
Pismis 13	7.950 (1), 7.800 (2), 8.285 (3), 7.794 (4)	2600 (1), 2926 (2), 2367 (3), 2668 (4)	0.028 (3)	2.046 (1), 1.670 (2), 1.916 (3)
Pismis 14	8.355 (1), 8.110 (2), 8.185 (3), 8.065 (4)	1775 (1), 1266 (2), 1234 (3), 1238 (4)	0.146 (3)	1.485 (1), 0.570 (2), 0.764 (3)
Pismis 15	9.095 (1), 8.940 (2), 9.258 (3), 8.652 (4)	2558 (1), 2559 (2), 1872 (3), 2254 (4)	−0.400 (1), 0.456 (3), 0.040 (5)	1.550 (1), 1.890 (2), 1.560 (3)
Pismis 18	8.975 (1), 8.760 (2), 8.832 (3), 8.509 (4)	2309 (1), 2860 (2), 2189 (3), 2598 (4)	−0.033 (3), 0.14 (5)	1.615 (1), 1.810 (2), 2.165 (3)
Pismis 19	9.015 (1), 8.920 (2), 8.046 (3), 8.090 (4)	1978 (1), 3515 (2), 1983 (3), 3034 (4)	0.064 (3)	4.033 (1), 3.660 (2), 1.743 (3)

Note. Values are listed in chronological order of the references. (1) Kharchenko et al. (2013); (2) Cantat-Gaudin et al. (2020); (3) Dias et al. (2021); (4) Hunt & Reffert (2024). (5) Randich et al. (2022).

2.3. Sample Selection: From 24 to 14 Clusters

The original Pismis catalog lists 24 open clusters. We evaluated the full list by applying the UPMASK membership algorithm detailed in Section 3.1 to the quality-filtered Gaia DR3 data of Section 2.1; this algorithm assigns each star a membership probability P. As shown in the preliminary CMD grid (Figure 1), several clusters were excluded from further analysis because they did not yield a sufficient number of members at a probability threshold of $P \geqslant 0.75$, or because their main sequences remained too heavily blended with field-star contamination for reliable isochrone fitting. This filtering left a final sample of 14 systems, selected on the basis of membership statistics and CMD morphology.

The specific causes for exclusion vary across the omitted systems. For instance, Pismis 16 yielded no member stars ($N_{0.75} = 0$) at our high-probability threshold, while Pismis 10 provided too few candidates ($N_{0.75} = 7$) to form a statistically significant sequence. Conversely, systems such as Pismis 20, 21, 22, and 23 displayed higher member counts but exhibited severe field star contamination that completely blended with the cluster main sequences. Pismis 24 presented a different observational challenge, as it is embedded within a dense nebulous region where high interstellar extinction obscures the cluster sequence on the CMD. Three further systems were removed for reasons specific to the fit rather than to the membership analysis. For Pismis 17 the UPMASK probability distribution failed to separate into cluster and field populations, remaining essentially flat between 0 and 1, and only ∼15 stars survived the quality cuts at the threshold used for the fits—too few to constrain an isochrone. For Pismis 2 the reddening posterior converged on the upper boundary of its prior, $E(G_{BP} - G_{RP}) = 1.5$ mag, indicating that the extinction was not constrained by the data and that the associated age and distance could not be trusted. Pismis 11 lies in a crowded, heavily obscured field in which the recovered sequence could not be interpreted unambiguously. Together with the seven systems above, this accounts for all ten clusters of the original catalog that are not analysed here. These contamination and extinction effects, visible as grey points in Figure 1, introduce significant uncertainties that prevent the Bayesian Nested Sampling algorithm from reaching reliable convergence.

By excluding these poorly defined or heavily obscured systems, we focused the study on the 14 clusters that provide the most coherent stellar sequences. This selection restricts the analysis to the systems for which the member sequence can be isolated with confidence; the residual level of field contamination in each of the retained clusters is assessed quantitatively in Section 5.2. The equatorial and Galactic coordinates adopted for each of the 14 selected clusters are listed in Table 2.

3. Method

3.1. Membership Analyses and Astrometric Parameters

Cluster membership determination relies on isolating the co-moving stellar population from the background and foreground field stars (Castro-Ginard et al. 2022). Because members of a single open cluster share a common space velocity and distance, they form distinct overdensities within the Gaia astrometric space (Cantat-Gaudin et al. 2018). We utilize these coherent vector groupings in proper motion ($\mu_\alpha \cos\delta$, μ_δ) and the localized distributions in trigonometric parallax (ϖ) as the primary multidimensional criteria to separate true cluster stars from field interlopers (Monteiro et al. 2021; Hunt & Reffert 2023).

In this study, we utilized Gaia DR3 proper motions and parallaxes to isolate cluster members from the field population across the 14 Pismis systems. Membership probabilities were calculated using the Unsupervised Photometric Membership Assignment in Stellar Clusters (UPMASK) algorithm (Krone-Martins & Moitinho 2014) via the `pyUPMASK` Python package (Pera et al. 2021). The identified members form distinct overdensities in the Vector Point Diagrams (VPDs) and exhibit clear separation from the background field (see Table A1).

The UPMASK algorithm operates through an iterative, non-parametric process to detect spatial and kinematic overdensities within a multidimensional parameter space. In each iteration, the five-dimensional astrometric data (α, δ, $\mu_\alpha \cos\delta$, μ_δ, ϖ) undergo Principal Component Analysis (PCA) to decorrelate and rescale the parameters. We deliberately restrict this feature space to astrometry alone, excluding photometric quantities such as G and ($G_{BP} - G_{RP}$): since our subsequent isochrone fitting (Section 3.2) uses these same photometric observables as its primary constraint, selecting members along the same photometric axes would circularly bias the sample toward stars already close to an assumed isochrone, artificially suppressing genuine scatter and pre-main-sequence or evolved outliers. The algorithm then applies k-means clustering to partition the data set into k groups, where the hyperparameter k scales with the expected cluster size. For internal validation, the spatial concentration of each identified group is compared against a uniform distribution generated via a random shuffling approach. Groups that exhibit a significantly higher concentration than the random distribution at a specified significance level are flagged as potential cluster members.

To account for observational uncertainties in the Gaia DR3 catalog (Gaia Collaboration et al. 2023), we performed the resampling process over 100 independent iterations. In each cycle, the astrometric parameters of every star were randomly drawn from a Gaussian distribution scaled by their measured values and associated uncertainties. The final membership probability (P) for each star corresponds to the frequency with which it was flagged as a member across all iterations. The membership probability enters the analysis at two distinct

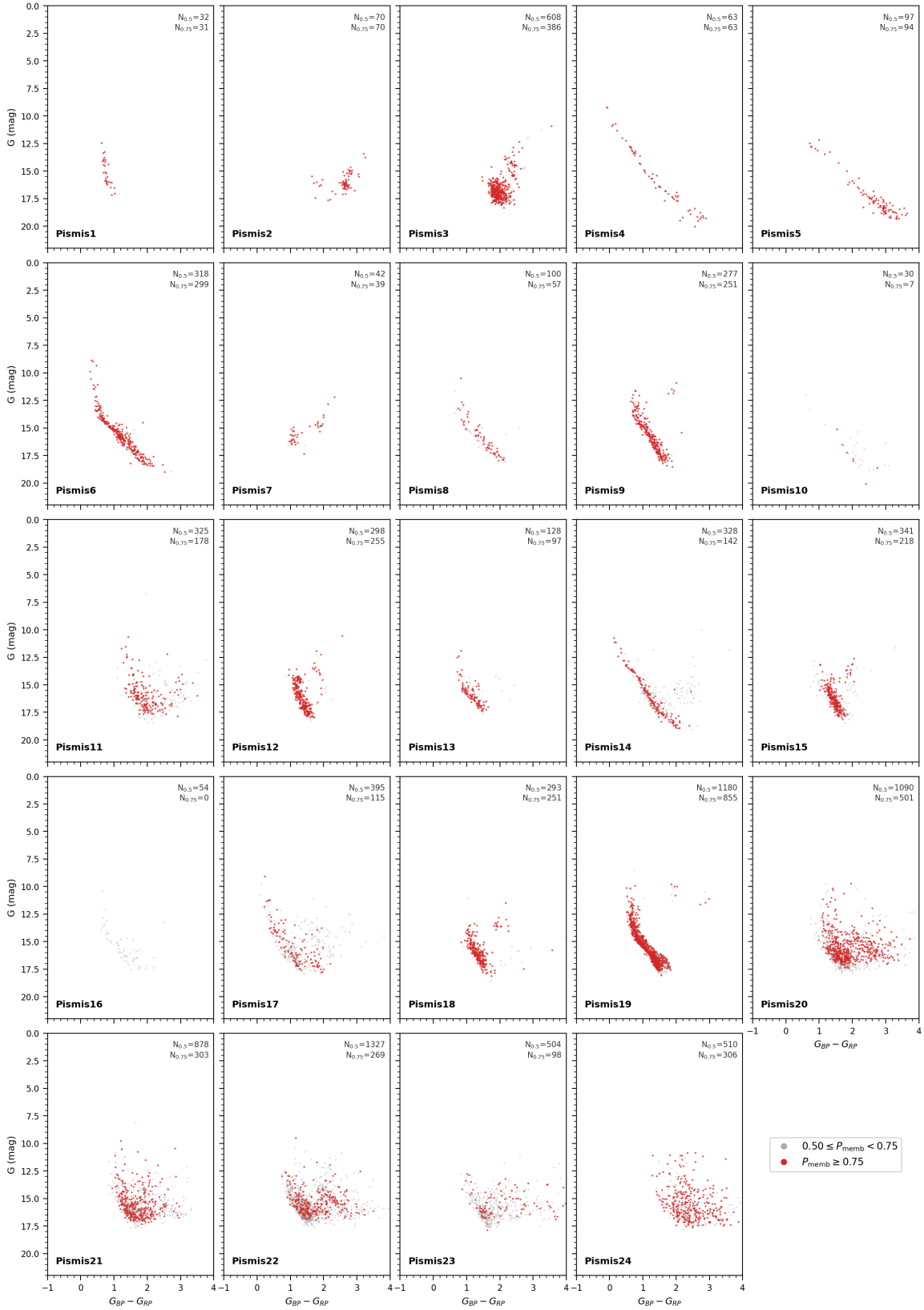


Figure 1. Color–Magnitude Diagrams (CMDs) for the initially surveyed Pismis clusters using Gaia DR3 photometry. The G versus ($G_{\rm BP} - G_{\rm RP}$) planes illustrate the clear separation between identified cluster members (highlighted in red) and the surrounding field star population. This preliminary grid served as the basis for our selection process, allowing us to identify systems with statistically significant membership counts and well-defined stellar sequences suitable for high-precision isochrone fitting.

Table 2
Equatorial (J2000) and Galactic Coordinates of the Selected Pismis Clusters

Cluster	R.A. (J2000)	Decl. (J2000)	l (deg)	b (deg)
Pismis 1	08:18:18.8	−37:06:06	255.1149	−0.7100
Pismis 3	08:31:20.4	−38:38:16	257.8519	0.5049
Pismis 4	08:35:09.6	−44:25:26	262.9290	−2.3630
Pismis 5	08:37:37.1	−39:35:23	259.3432	0.9119
Pismis 6	08:39:07.9	−46:13:36	264.7900	−2.8929
Pismis 7	08:41:08.2	−38:41:58	259.0520	1.9951
Pismis 8	08:41:36.2	−46:16:01	265.0830	−2.5789
Pismis 9	08:42:56.2	−44:55:55	264.1733	−1.5739
Pismis 12	09:20:01.4	−45:07:57	268.6539	3.2080
Pismis 13	09:22:07.0	−51:06:06	273.1240	−0.7650
Pismis 14	09:29:52.8	−52:46:48	275.1510	−1.1390
Pismis 15	09:34:44.7	−48:02:36	272.4989	2.8611
Pismis 18	13:36:54.8	−62:05:29	308.2260	0.3120
Pismis 19	14:30:40.0	−60:53:21	314.7100	−0.3070

Note. Right ascension and declination are given in sexagesimal units, while Galactic coordinates are in degrees.

Table 3
The Adopted k Parameter for the PYUPMASK Analysis and the Resulting Number of Member Stars ($N_{\rm mem}$) for the 14 Pismis Clusters, at the Uniform Membership Threshold $P \geqslant 0.90$ Used for the Isochrone Fits (Section 3.1)

Cluster Name	$k_{\rm means}$	$N_{\rm mem}$
Pismis 1	26	28
Pismis 3	11	120
Pismis 4	26	62
Pismis 5	10	90
Pismis 6	21	259
Pismis 7	11	38
Pismis 8	21	49
Pismis 9	11	193
Pismis 12	11	219
Pismis 13	8	86
Pismis 14	12	88
Pismis 15	16	182
Pismis 18	16	232
Pismis 19	9	571

stages, and with two different thresholds. The first is the assessment of which clusters can be analysed at all (Section 2.3): there we count members at $P \geqslant 0.75$, a threshold low enough that a system failing it cannot be said to possess a recoverable sequence, and we use those counts—together with the CMD morphology—to reduce the original catalog from 24 systems to 14. The second is the construction of the member samples that enter the isochrone fits themselves. For these we apply a uniform, more stringent cut of $P \geqslant 0.90$ to all 14 clusters, well above the $P > 0.5$ baseline common in the literature. The stricter cut is adopted deliberately: because every one of these systems lies close to the Galactic plane, sample purity rather than completeness is the limiting factor for isochrone fitting, and a uniform threshold keeps the 14 member catalogs mutually comparable, which a cluster-by-cluster optimisation would not. The member counts $N_{\rm mem}$ quoted throughout the paper and listed in Table 3 and Table 4 are therefore those at $P \geqslant 0.90$, whereas the counts used for the selection decision in Section 2.3 are those at $P \geqslant 0.75$; the catalog cross-matching of Section 4.2 uses a deliberately inclusive list ($P \geqslant 0.5$) so that the comparison is not biased by our own purity cut.

To maximize the purity of our final member list and mitigate the impact of unresolved binary systems, we applied a strict quality cut of RUWE < 1.4. This criterion effectively filters out sources with poorly constrained astrometric solutions, which are frequently associated with binary companions or spurious detections (Lindegren et al. 2018, 2021). Adopting RUWE as a metric for astrometric stability ensures a clean sample of stars suitable for precise isochrone fitting without requiring arbitrary photometric adjustments. Additionally, the final membership was restricted to stars within the observationally determined limiting radius ($r_{\rm lim}^{\rm obs}$). The complete set of astrometric and derived fundamental parameters for all 14 Pismis clusters is provided in Table A1.

3.2. Age Determination

Theoretical isochrones were computed using the PARSEC stellar evolution models (Bressan et al. 2012) accessed through the CMD 3.9 web interface,[6] adopting the Gaia DR3 photometric system (Gaia Collaboration et al. 2023). The grid spans $\log(\mathrm{Age/yr}) \in [6.0,\ 10.1]$ in steps of 0.05 dex (72 values), denoted log(Age) throughout the remainder of this paper for brevity, and initial metallicity $Z_{\rm ini}$ over 26 values distributed log-linearly between $Z = 0.0001$ ($[\mathrm{Fe/H}] \approx -2.18$) and $Z = 0.0500$ ($[\mathrm{Fe/H}] \approx +0.52$), with the solar value $Z_\odot = 0.0152$ explicitly included.

To enable rapid likelihood evaluations, we trained a SCIKIT-LEARN `DecisionTreeRegressor` as a high-dimensional interpolator on the grid, mapping the input triplet (log(Age), $Z_{\rm ini}$, $M_{\rm ini}$) to the observed Gaia quantities (G, $G_{\rm BP} - G_{\rm RP}$). Photometric extinction was applied following Wang & Chen (2019), using the coefficients $A_G/E(G_{\rm BP} - G_{\rm RP}) = 1.890$ and $E(G_{\rm BP} - G_{\rm RP})/E(B - V) = 1.305$.

We infer four global cluster parameters $\boldsymbol{\theta} = (\log(\mathrm{Age}), Z_{\rm ini}, d_{\rm pc}, E(G_{\rm BP} - G_{\rm RP}))$ via Dynamic Nested Sampling (Higson et al. 2019) using the DYNESTY package (Speagle 2020). The sampling was performed with 200 live points, employing a `multi`-ellipsoid bounding strategy and random-walk proposals (`rwalk`). Convergence was strictly defined by the evidence tolerance criterion $\Delta \ln \mathcal{Z} \leqslant 0.01$, where $\mathcal{Z}$ denotes the Bayesian evidence and is not to be confused with the initial metallicity $Z_{\rm ini}$ introduced above. Earlier versions of

[6] http://stev.oapd.inaf.it/cmd

Table 4
Bayesian Nested-sampling Parameters for 14 Pismis Open Clusters (PARSEC Isochrones)

Cluster	$N_{\rm mem}$	log(Age)	Age (Gyr)	$Z_{\rm ini}$	[Fe/H] (dex)	d (pc)	$E(G_{\rm BP}-G_{\rm RP})$
Pismis 1	28	$7.75^{+0.20}_{-0.21}$	$0.056^{+0.032}_{-0.021}$	$0.0092^{+0.0045}_{-0.0033}$	$-0.22^{+0.17}_{-0.19}$	5445^{+14}_{-15}	$0.955^{+0.040}_{-0.045}$
Pismis 3	120	$9.04^{+0.18}_{-0.21}$	$1.104^{+0.553}_{-0.430}$	$0.0111^{+0.0066}_{-0.0043}$	$-0.14^{+0.20}_{-0.21}$	2293^{+15}_{-15}	$1.575^{+0.142}_{-0.143}$
Pismis 4	62	$8.35^{+0.55}_{-0.50}$	$0.224^{+0.580}_{-0.154}$	$0.0084^{+0.0047}_{-0.0033}$	$-0.26^{+0.19}_{-0.21}$	690^{+15}_{-15}	$0.265^{+0.246}_{-0.143}$
Pismis 5	90	$7.04^{+0.50}_{-0.48}$	$0.011^{+0.024}_{-0.007}$	$0.0098^{+0.0052}_{-0.0038}$	$-0.19^{+0.19}_{-0.22}$	926^{+14}_{-15}	$0.600^{+0.253}_{-0.250}$
Pismis 6	259	$7.88^{+0.41}_{-0.55}$	$0.076^{+0.117}_{-0.054}$	$0.0100^{+0.0050}_{-0.0037}$	$-0.18^{+0.18}_{-0.20}$	1815^{+15}_{-15}	$0.736^{+0.162}_{-0.119}$
Pismis 7	38	$8.64^{+0.32}_{-0.11}$	$0.433^{+0.464}_{-0.095}$	$0.0092^{+0.0054}_{-0.0034}$	$-0.22^{+0.20}_{-0.20}$	5367^{+15}_{-15}	$1.075^{+0.085}_{-0.211}$
Pismis 8	49	$8.28^{+0.43}_{-0.53}$	$0.191^{+0.322}_{-0.135}$	$0.0108^{+0.0056}_{-0.0043}$	$-0.15^{+0.18}_{-0.22}$	1865^{+16}_{-15}	$0.981^{+0.167}_{-0.148}$
Pismis 9	193	$8.30^{+0.32}_{-0.46}$	$0.200^{+0.216}_{-0.131}$	$0.0111^{+0.0064}_{-0.0044}$	$-0.14^{+0.20}_{-0.22}$	1995^{+16}_{-14}	$0.928^{+0.134}_{-0.136}$
Pismis 12	219	$9.18^{+0.30}_{-0.17}$	$1.518^{+1.505}_{-0.492}$	$0.0104^{+0.0049}_{-0.0036}$	$-0.17^{+0.17}_{-0.19}$	2233^{+15}_{-15}	$0.798^{+0.146}_{-0.126}$
Pismis 13	86	$8.35^{+0.26}_{-0.30}$	$0.221^{+0.186}_{-0.110}$	$0.0176^{+0.0052}_{-0.0061}$	$+0.06^{+0.11}_{-0.19}$	2900^{+15}_{-15}	$0.919^{+0.091}_{-0.114}$
Pismis 14	88	$8.78^{+0.36}_{-0.39}$	$0.606^{+0.775}_{-0.357}$	$0.0097^{+0.0048}_{-0.0039}$	$-0.20^{+0.17}_{-0.22}$	1291^{+15}_{-14}	$0.442^{+0.119}_{-0.107}$
Pismis 15	182	$9.09^{+0.35}_{-0.21}$	$1.239^{+1.513}_{-0.467}$	$0.0124^{+0.0062}_{-0.0044}$	$-0.09^{+0.18}_{-0.19}$	2421^{+14}_{-16}	$0.969^{+0.155}_{-0.165}$
Pismis 18	232	$8.54^{+0.32}_{-0.43}$	$0.346^{+0.383}_{-0.217}$	$0.0143^{+0.0060}_{-0.0060}$	$-0.03^{+0.15}_{-0.24}$	2807^{+15}_{-14}	$1.160^{+0.135}_{-0.187}$
Pismis 19	571	$7.69^{+0.52}_{-0.55}$	$0.049^{+0.114}_{-0.035}$	$0.0103^{+0.0060}_{-0.0041}$	$-0.17^{+0.20}_{-0.22}$	2400^{+14}_{-15}	$0.799^{+0.189}_{-0.340}$

Note. Columns list: number of member stars after quality cuts ($N_{\rm mem}$), logarithmic age, age in Gyr, initial metallicity $Z_{\rm ini}$, iron abundance [Fe/H], heliocentric distance d, and reddening $E(G_{\rm BP}-G_{\rm RP})$. All values are posterior medians; uncertainties are 16th/84th percentile intervals.

this isochrone-fitting framework have been applied in previous open-cluster studies (Karagöz et al. 2025; Tanık Öztürk et al. 2025; Yontan et al. 2026).

For each proposed parameter set $\boldsymbol{\theta}$, a synthetic colour–magnitude diagram (CMD) is generated from the trained interpolator. Each observed star i is matched to its closest counterpart on the theoretical isochrone in the $(G_{\rm BP}-G_{\rm RP},\ G)$ plane. Denoting by $\sigma_{c,i}$ and $\sigma_{G,i}$ the observed photometric uncertainties in colour and magnitude, respectively, we define the squared distance χ^2_i as:

$$\chi^2_i(\boldsymbol{\theta}) = \frac{[(G_{\rm BP}-G_{\rm RP})_{{\rm obs},i} - (G_{\rm BP}-G_{\rm RP})_{\rm mod}]^2}{\sigma^2_{c,i}} + \frac{[G_{{\rm obs},i} - G_{\rm mod}]^2}{\sigma^2_{G,i}}, \quad (1)$$

To account for unmodelled systematics, potential binary sequences, and small-scale imperfections in stellar models, these uncertainties were inflated by a factor of 2.5. The final membership-weighted, truncated log-likelihood is given by:

$$\ln \mathcal{L}(\boldsymbol{\theta}) = -\frac{1}{2}\sum_i w_i \left[\min\left(\chi^2_i,\ \chi^2_{\rm max} \right) + \ln\left(2\pi\ \sigma_{c,i}\ \sigma_{G,i}\right) \right], \quad (2)$$

where $w_i = P_{{\rm mem},i}/\sum_j P_{{\rm mem},j}$ is the normalised UPMASK membership probability of star i, and $\chi^2_{\rm max} = 50$ is a robustness threshold applied to prevent runaway contributions from outliers or remaining field contaminants. The weighting was applied exclusively to member stars that exceeded the selected probability threshold ($P \geqslant P_{\rm threshold}$).

Each of the four free parameters is assigned a physically motivated prior as follows:

Age. In the absence of strong prior constraints on the age of each cluster, we adopt a non-informative uniform prior over the full range of the isochrone grid: $\pi(\log(\mathrm{Age})) = \mathcal{U}(6.0,\ 10.0)$. This ensures the posterior is driven primarily by the CMD morphology.

Metallicity. Given the lack of spectroscopic data for most Pismis clusters, we model the metallicity prior based on the distribution of solar-neighbourhood open clusters (Netopil et al. 2016). We adopt a skew-normal distribution:

$$\pi([\mathrm{Fe/H}]) \propto \mathrm{SN}(\mu = 0.0,\ \sigma = 0.3,\ \alpha = -2), \quad (3)$$

which accounts for the observed asymmetry and the preference for near-solar values. The sampled [Fe/H] is converted to $Z_{\rm ini}$ using $Z = Z_\odot\, 10^{[\mathrm{Fe/H}]}$.

Distance. We utilize Gaia DR3 parallaxes to anchor the distance scale. For stars satisfying quality cuts ($\varpi > 0$, $\sigma_\varpi/|\varpi| \leqslant 0.20$, RUWE $\leqslant 1.4$), we adopt a truncated Gaussian prior:

$$\pi(d) \propto \mathcal{N}(\tilde{d},\ 15^2)\ |_{d>0}, \quad (4)$$

where $\tilde{d}$ is the median distance derived from the cluster members. This informative, cluster-specific prior differs in form from the exponentially decreasing space-density prior of Bailer-Jones et al. (2021), which is designed for individual field stars with a single, often noisy parallax measurement and therefore requires a broad, direction-dependent length-scale prior to regularise the inversion. In our case, the prior mean $\tilde{d}$ is itself the median of tens to hundreds of parallaxes from co-distant cluster members, which already reduces the per-star parallax uncertainty by a factor of

order $\sqrt{N_{\rm mem}}$; the narrow 15 pc width reflects the residual uncertainty in this already well-constrained mean rather than an assumed astrophysical distance distribution. The two approaches are therefore consistent in spirit—both regularise the parallax-to-distance inversion with a prior appropriate to the information at hand—but ours is tailored to the more constrained problem of a resolved, multi-member cluster rather than a single field star. We note that neither $\tilde{d}$ nor the individual member parallaxes feeding into it were corrected for the Gaia DR3 parallax zero-point offset (e.g., Lindegren et al. 2021) or reprocessed through the Bailer-Jones et al. (2021) distance-estimation pipeline; the quoted distances and their uncertainties therefore reflect only the internal statistical precision of the Bayesian posterior and do not explicitly propagate this external systematic. Given the typical magnitude of the zero-point offset (∼10–40 μas, corresponding to a few percent in distance at the distances of our sample) relative to the 15 pc prior width and the posterior uncertainties reported in Table 4, we expect this to be a subdominant, though not negligible, source of additional systematic uncertainty, particularly for the most distant clusters in the sample (e.g., Pismis 1 and 7, at ∼5.4 kpc).

Reddening. The reddening $E(G_{\rm BP} - G_{\rm RP})$ is assigned a broad uniform prior $\pi(E) = \mathcal{U}(0.0,\ 5.0)$. To optimize the initial state of the nested sampler, we provide a starting estimate $\hat{E}_{\rm SFD}$ using Schlegel et al. (1998) dust maps via MWDUST(Bovy et al. 2016), corrected for a Galactic scale height of $h = 125$ pc.

4. Results

4.1. Derived Astrophysical Parameters and Statistical Diagnostics for Pismis 18

In this section, we present the fundamental parameters derived for our cluster sample. Pismis 18 is treated as a representative case, while the diagnostic plots and parameters for the remaining 13 clusters are provided as online supplementary material (see Data Availability). Figure 2 displays the posterior distributions alongside the corresponding isochrone fit. As shown in the Colour–Magnitude Diagram (top-right panel), stars with high membership probabilities ($P \geqslant 0.90$) define a well-defined Main Sequence. The median isochrone (orange solid line) and the 1σ uncertainty envelope (green dashed lines) are highly consistent with the observed data, particularly near the turn-off point. We determine the cluster age to be $\log(\mathrm{Age}) = 8.54^{+0.32}_{-0.43}$ (∼346 Myr).

4.1.1. Posterior Distributions and Parameter Degeneracies

The multidimensional parameter space—comprising age, metallicity (Z), distance ($d_{\rm pc}$), and interstellar reddening ($E(G_{\rm BP} - G_{\rm RP})$)—reveals the standard interdependencies inherent to isochrone fitting. The projected two-dimensional posterior contours in the corner plot display the structure of the likelihood surface for Pismis 18. A clear anti-correlation between log(Age) and $E(G_{\rm BP} - G_{\rm RP})$ is evident, reflecting the well-known degeneracy between cluster age and interstellar extinction. Despite this coupling, the Nested Sampling algorithm provides well-constrained posterior probability distributions, resolving the high-probability parameter space without introducing significant systematic offsets in the final estimates.

This results in a well-defined peak for the cluster age, indicating that for Pismis 18 the likelihood constrains age and reddening separately despite their correlation; we show in Section 5.2 that this separation is less effective for the differentially reddened systems of the sample. Regarding the spatial parameters, our analysis yields a heliocentric distance of $d = 2807^{+15}_{-14}$ pc. The symmetric, near-Gaussian profile of the distance posterior reflects the direct constraint provided by the Gaia DR3 parallaxes at kiloparsec scales. Furthermore, although the metallicity ($Z \approx 0.014$) was initially constrained by a skew-normal prior, the final posterior is shaped by the photometric likelihood; however, the metallicity constraints remain partially prior-dependent due to the limited sensitivity of Gaia broadband photometry to abundance variations. This convergence aligns Pismis 18 with the expected chemical properties of the Galactic disc. The parameters derived for Pismis 18 demonstrate the applicability of this framework to open clusters across diverse Galactocentric environments. Detailed diagnostic outputs for the remaining 13 clusters in our sample are documented as online supplementary material (see Data Availability).

4.2. Comparison with Previous Catalogs

4.2.1. Comparison of Membership Samples

We performed a cross-match between the members identified in this study and the established catalogs of Cantat-Gaudin et al. (2020; CG20) and Hunt & Reffert (2023; H23) using a matching radius of $r = 2''$. The resulting comparison matrix (Figure 3) provides the star recovery percentages and the Jaccard index, defined as $J = |A \cap B|/|A \cup B|$, i.e. the size of the intersection between two membership sets A and B divided by the size of their union, for each system.

The most notable feature of the comparison is the high number of unique members recovered in this study, particularly for clusters like Pismis 18 and Pismis 19. While our sample includes a significant majority of stars found in CG20 (with recovery rates reaching or exceeding 70% in six of the ten clusters for which CG20 provides a counterpart, and surpassing 90% in Pismis 7, 8, 12, 15, and 18), our total counts (TS) are significantly higher. The effect is most extreme for Pismis 19, the most crowded field in the sample, where the overlap with CG20 falls to a few per cent of our member list. This discrepancy indicates that global automated pipelines

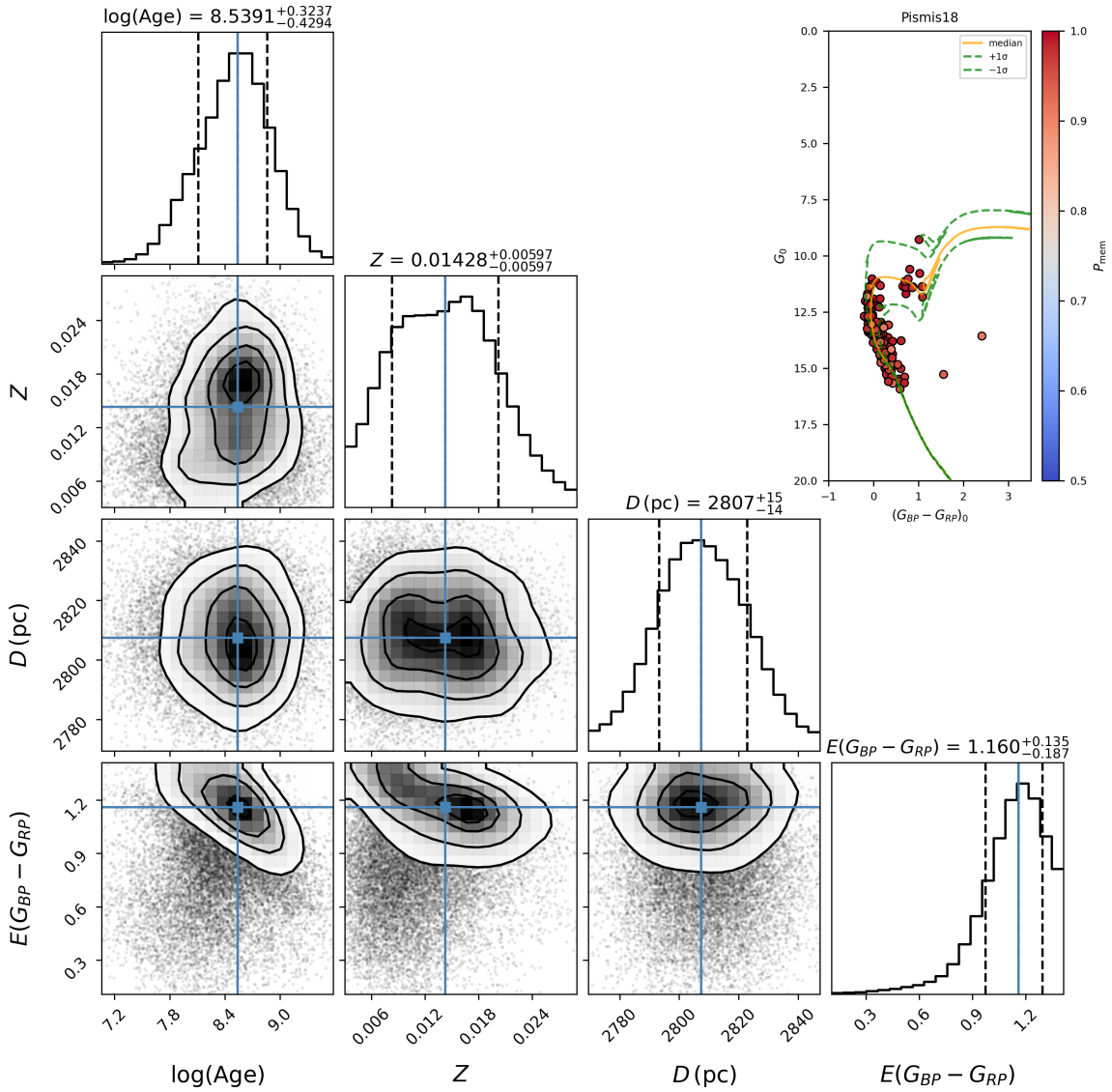


Figure 2. Bayesian parameter estimation results for the representative cluster Pismis 18. The projection matrix displays the one- and two-dimensional posterior probability distributions for the logarithmic age (log(Age)), metallicity (Z), heliocentric distance (D), and interstellar reddening ($E(G_{\rm BP} - G_{\rm RP})$). In the 2D covariance contours, the shaded regions represent the 1σ, 2σ, and 3σ confidence levels, respectively. The top-right panel illustrates the G versus $(G_{\rm BP} - G_{\rm RP})$ colour–magnitude diagram (CMD), with stars colour-coded according to their UPMASK membership probabilities. The best-fit PARSEC isochrone is denoted by a solid orange line, while green dashed lines represent the 1σ uncertainty envelope derived from the posterior samples.

likely omit a substantial portion of the cluster population in dense Galactic fields.

Additionally, Figure 3 shows low consistency between CG20 and H23 for several clusters, such as Pismis 8 and Pismis 19. In the case of Pismis 22 and 23, the recovery rate between our study and previous catalogs is effectively zero. This lack of overlap supports our decision to exclude these systems from the final astrophysical parameter estimation, as the high field contamination prevents reliable membership assignment even at the $P \geqslant 0.75$ level. These results demonstrate that cluster-specific analysis is required to obtain a complete census of the member population, especially for systems located in crowded regions.

4.3. Astrophysical Parameters and Bayesian Uncertainty Analysis

4.3.1. Comparison of Astrophysical Parameters

We compared the fundamental parameters derived in this study—log(Age), distance, and reddening—with the values from Cantat-Gaudin et al. (2020) for the 14 clusters in common. Figure 4 shows these comparisons, where points are

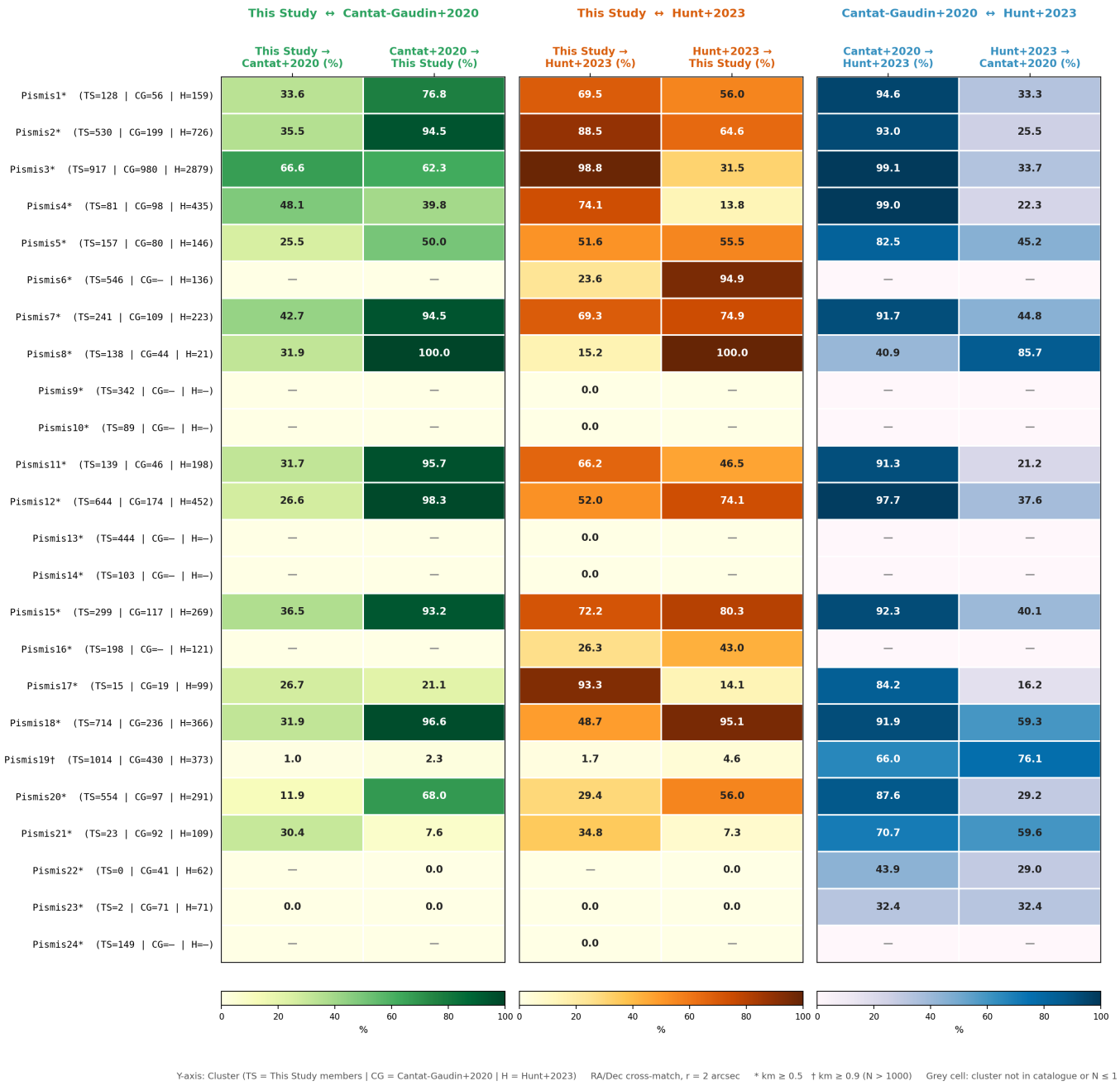


Figure 3. Membership comparison matrix across this work and established catalogs for the 24 Pismis clusters. Each cell provides the cross-match count (top), the Jaccard index ($J = |A \cap B|/|A \cup B| \times 100$, color-coded), and the percentage of star recovery between samples (bottom). The significant population of unique members identified in this study highlights the efficacy of cluster-specific analysis in revealing stellar populations previously missed by large-scale automated surveys.

color-coded according to the Jaccard similarity index. The distance estimates are consistent with the literature, showing a mean offset of $\bar{\Delta} = -37.56$ pc and a standard deviation of $\sigma = 284.92$ pc.

The reddening $E(G_{BP} - G_{RP})$ shows a systematic offset of $+0.24$ mag relative to the Cantat-Gaudin et al. (2020) values. Similarly, our age estimates are systematically older by a mean of $\bar{\Delta} = +0.09$ dex ($\sigma = 0.36$). The scatter in the age and reddening panels correlates with the membership differences; clusters with lower Jaccard similarity indices exhibit larger deviations from the 1:1 identity line. These systematic shifts indicate that the inclusion of the unique member populations identified via our

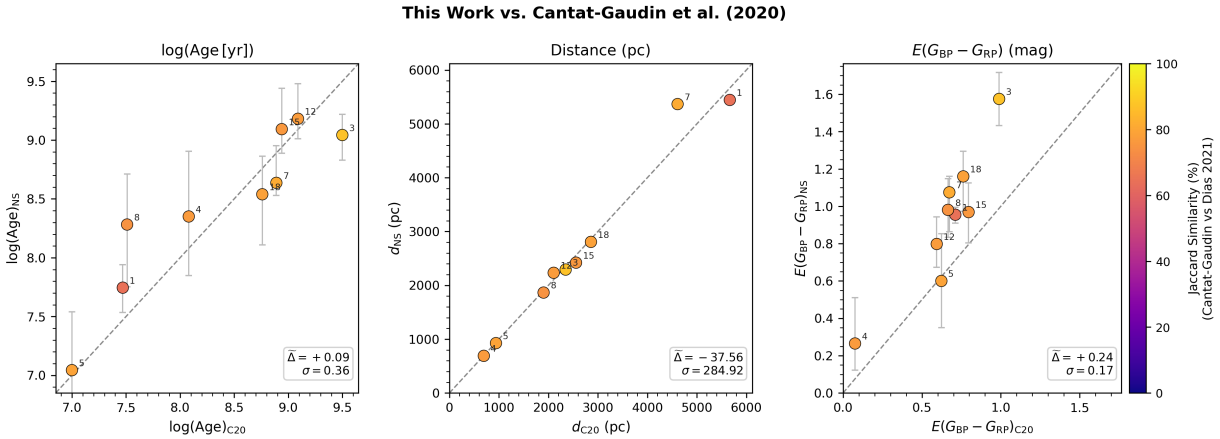


Figure 4. Comparison of fundamental parameters derived in this work with those from Cantat-Gaudin et al. (2020). Solid lines represent the 1:1 identity. Mean offsets (Δ) and standard deviations (σ) are indicated in each panel.

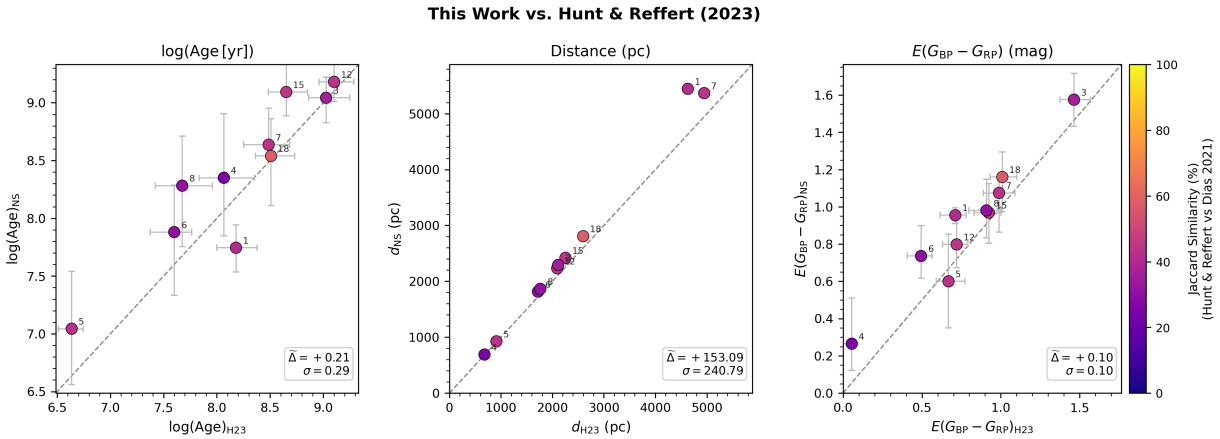


Figure 5. Same as Figure 4, but for comparison with the Hunt & Reffert (2023) catalog.

$P \geqslant 0.90$ threshold directly influences the results of the isochrone fitting process compared to automated global pipelines.

The astrophysical parameters for the 14 Pismis clusters, determined through Bayesian nested sampling, are presented in Table 4. Our approach provides not only the posterior medians but also the 16th and 84th percentile intervals, offering a rigorous assessment of the uncertainties associated with each parameter.

A similar comparison was performed with the results of Hunt & Reffert (2023) (H23), as shown in Figure 5. The distance estimates relative to H23 show a mean offset of $\bar{\Delta} = +153.09$ pc ($\sigma = 240.79$ pc). Our age estimates are also systematically older by $\bar{\Delta} = +0.21$ dex ($\sigma = 0.29$), while the reddening shows a systematic shift of $+0.10$ mag ($\sigma = 0.10$).

As indicated by the color-coding in Figure 5, the Jaccard similarity between this study and H23 is generally lower than that observed with CG20. The lower consistency in membership lists is evident in the age and distance panels, where clusters with the lowest similarity indices exhibit the largest deviations from the 1:1 identity line. These differences arise from the contrasting membership selection criteria and the choice of isochrone models between the two studies. The recovery of unique members in our analysis ($P \geqslant 0.90$) contributes to the observed offsets, confirming that astrophysical parameters are sensitive to the initial stellar population census in crowded Galactic regions.

We further compared our derived parameters with the results of Dias et al. (2021; D21) for 14 clusters. Figure 6 illustrates these comparisons, where points are color-coded according to the Jaccard similarity index. The distance estimates show a mean offset of $\bar{\Delta} = +173.70$ pc ($\sigma = 520.91$ pc), while log(Age) and reddening $E(G_{BP} - G_{RP})$ exhibit offsets of $+0.13$ dex ($\sigma = 0.47$) and $+0.16$ mag ($\sigma = 0.14$), respectively.

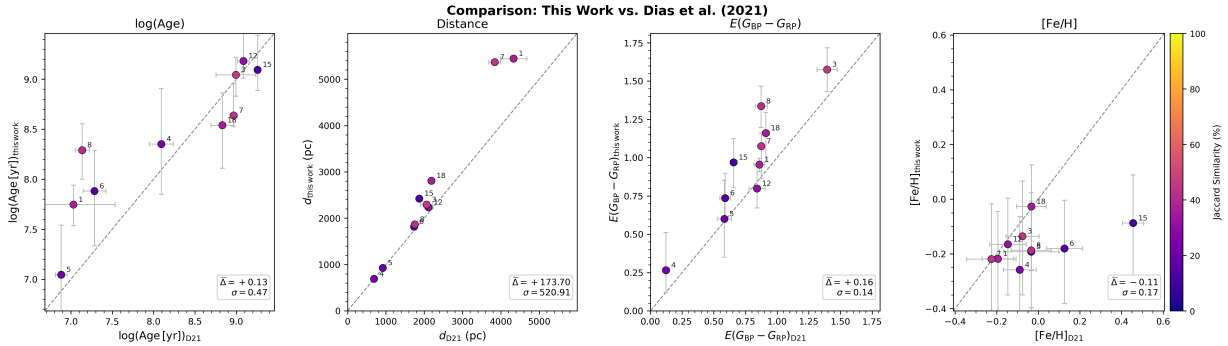


Figure 6. Comparison of age, distance, reddening, and metallicity ([Fe/H]) with Dias et al. (2021). This comparison highlights the significant dispersion in photometric metallicity estimates across different pipelines.

The comparison of metallicity ([Fe/H]) reveals a mean offset of -0.11 dex with a dispersion of $\sigma = 0.17$ dex. Since the estimates in D21 are derived photometrically, they are sensitive to the age-reddening-metallicity degeneracy. Our Bayesian framework, utilizing the $P \geqslant 0.90$ membership threshold, provides a more constrained fit by incorporating the unique member populations identified in this study. The discrepancies observed in Figure 6, particularly for clusters with low Jaccard similarity such as Pismis 15, indicate that the resulting photometric metallicity is highly dependent on the initial membership selection and the resulting morphology of the CMD. The inclusion of these unique members allows for a more precise definition of the cluster sequences, thereby refining the astrophysical parameters compared to automated global pipelines.

Age and Evolutionary Status. The sample covers a broad age range, spanning from very young systems to intermediate-age open clusters. Pismis 5 ($\log(\mathrm{Age}) \approx 7.04$) and Pismis 19 ($\log(\mathrm{Age}) \approx 7.69$) are identified as the youngest clusters, with ages below 50 Myr. Conversely, Pismis 12 ($1.52^{+1.51}_{-0.49}$ Gyr) and Pismis 15 ($1.24^{+1.51}_{-0.47}$ Gyr) represent the oldest population in the sample.

The age uncertainties for several young clusters, such as Pismis 4, 5, and 19, exhibit significant asymmetry. This phenomenon is a direct consequence of the CMD morphology in young populations, where the Main Sequence Turn-Off (MSTO) is not yet clearly defined, and the luminosity of the brightest members carries a degenerate relationship between age and extinction. For Pismis 4, the large upper uncertainty ($0.224^{+0.580}_{-0.154}$ Gyr) highlights the inherent difficulty in precisely dating the upper MS when post-MS evolutionary phases are sparsely populated.

Metallicity and Chemical Trends. The initial metallicities (Z_{ini}) of the clusters predominantly indicate sub-solar values, with an average iron abundance of $[\mathrm{Fe/H}] \approx -0.15$ dex. Pismis 13 stands out as the most metal-rich system in the sample, showing a super-solar median of $[\mathrm{Fe/H}] = +0.06^{+0.11}_{-0.19}$ dex. The uncertainties in metallicity, typically around ± 0.2 dex, reflect the well-known Z–Age–Reddening degeneracy in photometric isochrone fitting. These intervals are set by the sensitivity of Gaia broadband colours to abundance, and the metallicities should accordingly be read as loose photometric estimates rather than as substitutes for spectroscopy (Section 5.5).

Distance and Extinction. The heliocentric distances derived for the sample range from the relatively nearby Pismis 4 (690 ± 15 pc) to the distant Pismis 1 (5445^{+14}_{-15} pc) and Pismis 7 (5367^{+15}_{-15} pc). The quoted distance intervals are narrow, typically below 1%, but they are set by the width of the cluster-specific parallax prior described in Section 3.2 rather than by the photometric likelihood, and they should therefore be read as the internal precision of the fit given that prior, not as an independent measurement of the distance.

Line-of-sight reddening values $E(G_{\mathrm{BP}} - G_{\mathrm{RP}})$ exhibit high variability, peaking at $1.575^{+0.142}_{-0.143}$ for Pismis 3. Parameters are recovered for these high-extinction systems without the fit degrading: Pismis 3, the most reddened cluster in the sample, has the narrowest age posterior of all 14 (Section 5.2). This reflects the informative distance prior, which removes one direction of the age–distance–reddening degeneracy and leaves the photometry to constrain the remaining two.

5. Discussion

We have derived fundamental astrophysical parameters-age, heliocentric distance, interstellar extinction (A_V), and metallicity ([Fe/H])-for 14 poorly studied open clusters in the Pismis catalog. Using a Bayesian nested sampling analysis of Gaia DR3 data, we place these systems on a single, internally consistent parameter scale; the extent to which this reconciles the discrepant literature values is examined cluster by cluster below. Our sample exhibits significant physical diversity, with ages ranging from ∼11 Myr (Pismis 5) to ∼1.5 Gyr (Pismis 12) and distances extending to the outer disc periphery at ∼5.4 kpc (Pismis 1).

Pismis 1 stands out as an exceptionally young system (∼55 Myr) at a significant heliocentric distance ($d \approx 5.4$ kpc), indicating active star formation in the remote reaches of the outer disc. Similarly, Pismis 3 presents a case of extreme obscuration ($E(G_{BP} - G_{RP}) \approx 1.58$ mag) due to its precise location on the Galactic mid-plane, yet our framework successfully recovered its intermediate-age (1.1 Gyr) population. For the nearby but overlooked Pismis 4 and the Vela-associated Pismis 5, our results provide the first cluster-specific baselines, confirming Pismis 5's place within a primordial triple system (Qin et al. 2023). These findings establish a refined census of the Pismis clusters within the Galactic disc context, as detailed in the following subsections.

5.1. Comparison with Prior Studies: Cluster-by-Cluster Notes

In the following we discuss each of the 14 analysed clusters in turn, comparing our Bayesian nested-sampling results with the four major catalogs: Dias et al. (2021; hereafter D21), Cantat-Gaudin et al. (2020; hereafter CG20), Kharchenko et al. (2013; hereafter K13), and Hunt & Reffert (2024; hereafter HR24). We use the two successive releases of the Hunt & Reffert census for the two purposes to which each is best suited: the membership comparison of Section 4.2 adopts the all-sky member lists of Hunt & Reffert (2023; H23), whereas the parameter comparison below adopts the dynamically cleaned catalog of Hunt & Reffert (2024), in which the cluster sample has been filtered for physically bound systems and the fundamental parameters correspondingly revised. Where spectroscopic metallicity estimates or targeted photometric studies exist, we also compare against those dedicated works. Throughout, ages derived from our log(Age) posteriors are quoted in Myr unless otherwise stated, and heliocentric distances refer to the median of the posterior distribution.

5.1.1. Pismis 1

Our analysis yields $\log(\mathrm{Age}) = 7.75$ (56^{+32}_{-21} Myr), a heliocentric distance of 5445 ± 15 pc, and a reddening $E(G_{BP} - G_{RP}) = 0.95$ ($A_V \approx 2.27$ mag). The inferred metallicity is $[\mathrm{Fe/H}] = -0.22^{+0.17}_{-0.19}$ dex.

There is broad agreement in the distance among K13 (5903 pc), CG20 (5666 pc), and our result, while D21 (4333 pc) and HR24 (4630 pc) are systematically lower by ∼800–1100 pc. For the age, our $\log(\mathrm{Age}) = 7.75$ falls between CG20 (7.47) and K13 (7.80), whereas D21 reports a considerably younger value of 7.03 (∼11 Myr). The D21 age is likely underestimated given the large formal uncertainty ($\sigma = 0.50$ dex) they report for this cluster. HR24 gives a noticeably older $\log(\mathrm{Age}) = 8.18$ (∼150 Myr), which is inconsistent with the presence of early-type main-sequence stars expected at the distance and reddening of Pismis 1. Our extinction $A_V \approx 2.27$ mag is consistent with D21 (2.04 mag) and K13 (1.81 mag). The metallicity from D21, $[\mathrm{Fe/H}] = -0.19 \pm 0.08$ dex, is in excellent agreement with our posterior median of −0.22 dex.

5.1.2. Pismis 3

We derive $\log(\mathrm{Age}) = 9.04$ ($1.10^{+0.55}_{-0.43}$ Gyr), a distance of 2293 pc, and a reddening $E(G_{BP} - G_{RP}) = 1.57$ ($A_V \approx 3.74$ mag). The high extinction is consistent with the location of this cluster behind the Vela molecular complex.

Pismis 3 is one of the most robustly determined clusters in our sample, with D21 ($\log(\mathrm{Age}) = 9.00$, 2064 pc), K13 (8.93, 1418 pc), and HR24 (9.03, 2112 pc) all converging on an age near 1 Gyr. Our distance of 2293 pc is in good agreement with D21 and HR24, and particularly with CG20 (2349 pc). The strong outlier is K13, which places the cluster at only 1418 pc—roughly 800 pc closer—likely due to the use of 2MASS photometry, which is less sensitive to the upper main sequence in highly reddened fields (Tadross 2008). CG20 also stands apart with $\log(\mathrm{Age}) = 9.50$ (∼3.2 Gyr), significantly older than all other estimates; this may reflect the difficulty of the ANN method in separating the main-sequence turnoff from evolved field giants at this extinction level. Our extinction $A_V \approx 3.74$ mag agrees closely with D21 (3.31 mag) and K13 (3.68 mag). Our metallicity posterior, $[\mathrm{Fe/H}] = -0.14^{+0.20}_{-0.21}$ dex, is consistent with the slightly sub-solar value reported by D21 (-0.08 ± 0.08 dex).

5.1.3. Pismis 4

Our result for Pismis 4 is $\log(\mathrm{Age}) = 8.35$ (224^{+580}_{-154} Myr), a distance of 690 pc, and $E(G_{BP} - G_{RP}) = 0.26$ ($A_V \approx 0.63$ mag). The cluster is one of the nearest in the Pismis catalog and suffers little foreground reddening.

The distance estimate shows exceptional agreement across all catalogs: D21 (691 pc), CG20 (695 pc), K13 (575 pc), and HR24 (681 pc) all concur within ∼10%, and our value of 690 pc falls squarely among them (K13 somewhat low). The age is, however, slightly elevated relative to the literature consensus: D21, CG20, and HR24 all report $\log(\mathrm{Age}) \approx 8.07$–$8.08$ (∼118–120 Myr), and K13 gives 8.15. Our median of 8.35 (224 Myr) is ∼0.2 dex higher, though the broad posterior (16th–84th percentile range ∼70–800 Myr) means this is not a statistically significant discrepancy. The low extinction makes the main-sequence turnoff morphology the primary age discriminant, and the small membership sample ($N = 62$) increases the posterior width. The metallicity D21 reports (-0.09 ± 0.08 dex) is consistent with our $[\mathrm{Fe/H}] = -0.26^{+0.19}_{-0.21}$ dex, both pointing to a slightly sub-solar composition.

5.1.4. Pismis 5

Pismis 5 is one of the youngest clusters in our sample. We find $\log(\mathrm{Age}) = 7.04$ (11^{+24}_{-7} Myr), a distance of 926 pc, and $E(G_{\mathrm{BP}} - G_{\mathrm{RP}}) = 0.60$ ($A_V \approx 1.43$ mag).

The distance and age are in excellent agreement with D21 (6.88, 921 pc) and CG20 (7.00, 941 pc), and with HR24 (6.64, 913 pc). All four estimates confirm a young, nearby cluster with moderate reddening. The outlier is K13, which places the cluster at only 702 pc and assigns a considerably higher extinction ($A_V = 2.58$ mag)—a combination that is difficult to reconcile physically. Bonatto & Bica (2009) studied Pismis 5 in detail and concluded it belongs to the Vela molecular ridge star-forming region at a distance of ∼900 pc, consistent with our result. The molecular environment also explains the asymmetric posterior on the age: the upper bound is poorly constrained because the pre-main-sequence locus overlaps with background giant sequences at young ages. Our metallicity, $[\mathrm{Fe/H}] = -0.19^{+0.19}_{-0.22}$ dex, is marginally more sub-solar than the D21 value (-0.03 ± 0.13 dex), but is consistent within the uncertainties.

5.1.5. Pismis 6

We obtain $\log(\mathrm{Age}) = 7.88$ (76^{+117}_{-54} Myr) for Pismis 6 (also known as NGC 2645), a distance of 1815 pc, and $E(G_{\mathrm{BP}} - G_{\mathrm{RP}}) = 0.74$ ($A_V \approx 1.75$ mag).

Our age is systematically higher than all catalog values, which range from $\log(\mathrm{Age}) = 7.28$ (D21, ∼19 Myr) through 7.41 (CG20) and 7.58 (K13) to 7.60 (HR24, ∼40 Myr). Targeted studies are similarly young: Fitzgerald et al. (1979) report ∼1.7 kpc, consistent with our distance, while Forbes & Short (1994) derive an age of ∼8 Myr from UBV photometry. The factor of ∼3 discrepancy in age is notable. The presence of the luminous F0 Ia supergiant HD 74180 - physically associated with Pismis 6 (Fitzgerald et al. 1979; Forbes & Short 1994) - is a strong indicator of a very young cluster, as such supergiants evolve on timescales of only a few megayears. We speculate that the CMD morphology of Pismis 6 in Gaia DR3 is affected by differential reddening across the cluster face (as suggested by Fitzgerald et al. 1979), causing the apparent main-sequence turnoff to scatter toward redder colours and mimicking an older population. Deeper spectroscopic observations would be required to resolve this discrepancy.

An additional tension concerns the metallicity: D21 reports $[\mathrm{Fe/H}] = +0.13 \pm 0.09$ dex (super-solar), whereas our posterior yields $[\mathrm{Fe/H}] = -0.18^{+0.18}_{-0.20}$ dex (sub-solar). Given that no high-resolution spectroscopic study exists for this cluster, the D21 metallicity, which relies on low-resolution survey data, may carry underestimated systematic errors.

5.1.6. Pismis 7

For Pismis 7 we find $\log(\mathrm{Age}) = 8.64$ (433^{+464}_{-95} Myr), a distance of 5367 pc, and $E(G_{\mathrm{BP}} - G_{\mathrm{RP}}) = 1.07$ ($A_V \approx 2.55$ mag).

The age estimates from the literature span a moderate range: K13 (8.70), HR24 (8.49), CG20 (8.89), and D21 (8.97), with our value of 8.64 falling in the lower part of this range but remaining consistent with K13 and HR24 within uncertainties. Ahumada (2005) performed CCD photometry and also found an intermediate age consistent with $\log(\mathrm{Age}) \sim 8.7$. The most significant disagreement is in distance: our posterior places the cluster at 5367 pc, ∼400 pc beyond the most distant catalog estimate (HR24: 4947 pc) and ∼1.5 kpc beyond D21 (3843 pc). This may be linked to the high reddening and the difficulty of fitting the faint end of the main sequence without contamination by fore/background stars at this Galactic longitude. The metallicity, $[\mathrm{Fe/H}] = -0.22^{+0.20}_{-0.20}$ dex, is in near-perfect agreement with D21 (-0.225 ± 0.12 dex). Çakmak et al. (2021) independently studied cluster dynamics in this region and found consistent parameters.

5.1.7. Pismis 8

Pismis 8 presents one of the most significant age discrepancies within our sample. We derive $\log(\mathrm{Age}) = 8.28$ (191^{+322}_{-135} Myr), whereas all four literature catalogs favour substantially younger solutions: D21 (7.14, ∼14 Myr), K13 (7.43, ∼27 Myr), CG20 (7.51, ∼32 Myr), and HR24 (7.67, ∼47 Myr). A dedicated CCD $UBVI_c$ study by Giorgi et al. (2005) likewise supported a young evolutionary stage consistent with the literature consensus.

The distance determination is considerably more stable across studies. Our Bayesian solution (1865 pc) agrees well with D21 (1756 pc), CG20 (1903 pc), and HR24 (1765 pc), all of which remain consistent within ∼150 pc. Only K13 (1363 pc) yields a significantly shorter distance.

For the remaining parameters we obtain $E(G_{\mathrm{BP}} - G_{\mathrm{RP}}) = 0.98^{+0.17}_{-0.15}$ ($A_V \approx 2.33$ mag) and $[\mathrm{Fe/H}] = -0.15^{+0.18}_{-0.22}$ dex, the latter consistent with the near-solar composition found for the rest of the sample. The reddening is moderate but not negligible, and because extinction and age enter the CMD along nearly the same direction, part of the offset between our solution and the younger literature ages may reflect a different partitioning between the two: a bluer, less reddened solution would shift the inferred turn-off toward younger ages. The posterior itself does not resolve this, as the age and reddening uncertainties quoted above are correspondingly broad.

The origin of the age discrepancy is likely related to the sensitivity of the CMD morphology to the adopted membership selection. The young stellar indicators expected for a ∼10–50 Myr population—such as a clearly populated upper main sequence, OB-type stars, or pre-main-sequence

sequences—are not prominently visible in the final Gaia DR3 member sample adopted in this work. This may indicate that the brightest candidate members are either affected by field contamination, differential reddening, or were excluded during the high-probability membership filtering process.

Given the relatively sparse final membership ($N = 49$), the morphology of the upper main sequence remains weakly constrained, allowing multiple acceptable isochrone solutions across a broad age range. Consequently, the evolutionary status of Pismis 8 should be regarded as uncertain, and the older Bayesian solution presented here should be interpreted with caution until high-resolution spectroscopic membership confirmation becomes available for the brightest candidate stars.

5.1.8. Pismis 9

Our result for Pismis 9 is log(Age) = 8.30 (200^{+216}_{-131} Myr), a distance of 1995 pc, and $E(G_{BP} - G_{RP}) = 0.93$ ($A_V \approx 2.20$ mag).

The literature catalogs split into two groups: D21 (7.61, 1815 pc) and K13 (7.36, 1713 pc) report a significantly younger population (∼23–40 Myr), while CG20 (8.50, 2120 pc) and HR24 (8.46, 1865 pc) are considerably older and closer to our result. Our distance of 1995 pc is intermediate between the two groups, consistent with both CG20 and HR24. The bimodal age distribution across catalogs likely reflects the different photometric data sets and membership algorithms: D21 and K13 rely on pre-Gaia photometry, whereas CG20 and HR24 use Gaia DR2/DR3 astrometry. Our Gaia DR3–based analysis confirms the older solution. The metallicity [Fe/H] = $-0.14^{+0.20}_{-0.22}$ dex is consistent with D21 (-0.08 ± 0.14 dex) within the uncertainties.

5.1.9. Pismis 12

Pismis 12 shows the highest degree of consensus across all catalogs in our sample. We find log(Age) = 9.18 ($1.52^{+1.50}_{-0.49}$ Gyr), a distance of 2233 pc, and $E(G_{BP} - G_{RP}) = 0.80$ ($A_V \approx 1.90$ mag).

All four catalogs agree closely: D21 (9.09, 2114 pc), CG20 (9.09, 2107 pc), K13 (9.20, 2221 pc), and HR24 (9.10, 2094 pc). Our median log(Age) = 9.18 falls within this tight bracket. The distance is similarly consistent across all sources, ranging from 2094 to 2233 pc. The metallicity from D21, [Fe/H] = -0.15 ± 0.09 dex, matches our posterior, [Fe/H] = $-0.17^{+0.17}_{-0.19}$ dex, almost exactly. Pismis 12 is likely the most reliably determined cluster in the Pismis catalog, and it serves as an internal validation of the consistency between our Bayesian pipeline and the established literature.

5.1.10. Pismis 13

We derive log(Age) = 8.35 (221^{+186}_{-110} Myr) for Pismis 13, with a distance of 2900 pc and $E(G_{BP} - G_{RP}) = 0.92$ ($A_V \approx 2.18$ mag).

There is a clear split in the literature: D21 (8.29, 2367 pc) is the closest to our result and supports an intermediate age of ∼200 Myr, while CG20 (7.80, 2926 pc), K13 (7.95, 2600 pc), and HR24 (7.79, 2668 pc) all favour a much younger cluster (∼63–89 Myr). Our distance of 2900 pc agrees remarkably well with CG20 (2926 pc). Giorgi et al. (2005) studied both Pismis 8 and 13 simultaneously from CCD *UBVIc* photometry and derived physical parameters for Pismis 13 consistent with the younger solutions of CG20 and K13. Claria (1979) earlier reported a compact, old-looking cluster, but their analysis was based on photographic photometry. The intermediate age we recover may reflect the impact of field-star contamination: at a distance of ∼2.9 kpc along a modestly reddened line of sight, the cluster sequence can be confused with evolved foreground stars, making the turnoff appear at a fainter, redder location. The slightly super-solar metallicity, [Fe/H] = $+0.06^{+0.11}_{-0.19}$ dex, is consistent with D21 ($+0.028 \pm 0.096$ dex), supporting a somewhat metal-rich inner-Galaxy cluster.

5.1.11. Pismis 14

Our Bayesian analysis gives log(Age) = 8.78 (606^{+775}_{-357} Myr) for Pismis 14, a distance of 1291 pc, and $E(G_{BP} - G_{RP}) = 0.44$ ($A_V \approx 1.05$ mag).

The distance is well constrained and strongly consistent with D21 (1234 pc), CG20 (1266 pc), and HR24 (1238 pc); K13 (1775 pc) is the only outlier. The age, however, is substantially higher in our analysis than in the literature: D21 (8.19, ∼155 Myr), CG20 (8.11, ∼129 Myr), and HR24 (8.06, ∼115 Myr) all cluster around 120–160 Myr, while K13 gives a somewhat intermediate value of 8.35 (∼224 Myr). Our median of 8.78 (∼606 Myr) represents more than a factor of four increase in age. Given the relatively sparse membership ($N = 88$) and the moderate reddening, the main-sequence turnoff is not sharply defined; the broad posterior (∼0.25–1.4 Gyr at 1σ) reflects this genuine ambiguity. There is also a notable tension in metallicity: D21 reports [Fe/H] = $+0.15 \pm 0.10$ dex (super-solar), whereas our posterior gives [Fe/H] = $-0.20^{+0.17}_{-0.22}$ dex (sub-solar). A high-resolution spectroscopic study of confirmed members would be particularly valuable for this cluster.

5.1.12. Pismis 15

We find log(Age) = 9.09 ($1.24^{+1.51}_{-0.47}$ Gyr), a distance of 2421 pc, and $E(G_{BP} - G_{RP}) = 0.97$ ($A_V \approx 2.30$ mag) for Pismis 15.

The age is broadly consistent with K13 (9.10) and CG20 (8.94), and somewhat lower than D21 (9.26, ∼1.8 Gyr),

while HR24 gives a notably younger 8.65 (∼0.45 Gyr). For the distance, our 2421 pc is intermediate between D21 (1872 pc) and CG20/K13 (∼2558 pc). Carraro et al. (2005) performed a dedicated study and derived an age around 1–2 Gyr with a distance of ∼2 kpc, in general agreement with our results. The metallicity situation for Pismis 15 is remarkably discordant in the literature: D21 reports [Fe/H] = + 0.46 ± 0.05 dex (strongly super-solar), K13 gives −0.40 dex (strongly sub-solar), and our posterior yields [Fe/H] = $-0.09^{+0.18}_{-0.19}$ dex (near-solar). This large spread (∼0.9 dex peak-to-peak) suggests that the photometric metallicity estimates for this cluster are unreliable, and a spectroscopic determination is warranted.

5.1.13. Pismis 18

We obtain log(Age) = 8.54 (346^{+383}_{-217} Myr), a distance of 2807 pc, and $E(G_{BP} - G_{RP}) = 1.16$ ($A_V \approx 2.76$ mag) for Pismis 18.

Pismis 18 is the best-studied cluster of the sample, and the one for which the diagnostic plots are presented in the main text (Section 4). Its characterisation has evolved through successive observational regimes: the UBVI CCD photometry of Carraro & Seleznev (2012) established its place in the inner disc, after which it became the subject of dedicated spectroscopic work within the Gaia-ESO Survey (Hatzidimitriou et al. 2019) and of near-infrared imaging within the VVV Open Cluster Project (Baravalle et al. 2021; Peña Ramírez et al. 2021).

Pismis 18 is one of the few clusters in our sample with a published high-resolution spectroscopic study: Hatzidimitriou et al. (2019) used the Gaia-ESO Survey to derive a spectroscopic metallicity of [Fe/H] = +0.23 ± 0.05 dex from radial velocity members, and a cluster age of ∼700 Myr. Our metallicity posterior, [Fe/H] = $-0.03^{+0.15}_{-0.24}$ dex, is in good agreement with the Gaia-ESO value and with D21 (−0.033 ± 0.071 dex). However, our age (∼346 Myr) is significantly younger than the Gaia-ESO estimate and than the catalog values of D21 (8.83, ∼680 Myr), CG20 (8.76, ∼575 Myr), and K13 (8.98, ∼950 Myr). Only HR24 (8.51, ∼323 Myr) is consistent with our result. The distance is well reproduced by CG20 (2860 pc) and HR24 (2598 pc); D21 (2189 pc) and K13 (2309 pc) are systematically lower. The high reddening ($A_V \approx 2.76$ mag) may cause systematic biases in the photometric age determination if foreground extinction is non-uniform, and we note that the Gaia-ESO membership used by Hatzidimitriou et al. (2019) is more restrictive than our UPMASK-based membership. Peña Ramírez et al. (2021) studied Pismis 18 in the near-infrared with VVV and derived an age consistent with ∼1 Gyr.

The spread across these determinations—from ∼323 Myr to ∼1 Gyr for the same cluster—is itself informative, and is attributable to differences in membership selection, isochrone models and the treatment of extinction in a dense, reddened field. Baravalle et al. (2021) reported a substantial increase in the number of candidate members once multi-wavelength data were used, and the moderate overlap between our membership sample and those of CG20 and H23 (Figure 3) points to the same sensitivity: which faint stars are admitted to the sample largely determines the recovered turn-off, and hence the age.

5.1.14. Pismis 19

Pismis 19 is the most challenging cluster in our sample. We derive log(Age) = 7.69 (49^{+114}_{-35} Myr), a distance of 2400 pc, and $E(G_{BP} - G_{RP}) = 0.80$ ($A_V \approx 1.90$ mag).

Our age of ∼49 Myr is substantially younger than all literature estimates: D21 (8.05, ∼112 Myr), HR24 (8.09, ∼123 Myr), CG20 (8.92, ∼832 Myr), and K13 (9.02, ∼1.0 Gyr). The catalogs themselves disagree wildly, spanning nearly an order of magnitude in age, which already signals that Pismis 19 is a poorly constrained system. The distance estimates are equally scattered: D21/K13 place the cluster at ∼1980 pc, while CG20 (3515 pc) and HR24 (3034 pc) give considerably larger distances; our result of 2400 pc is intermediate. Reddening is also discrepant: CG20 (A_V = 3.66 mag) and K13 (4.03 mag) suggest heavy extinction, whereas D21 (1.74 mag) and our own estimate (1.90 mag) indicate only moderate absorption. The complexity of this system has been noted in the dedicated literature. Carraro & Munari (2004) performed multicolour CCD photometry and found evidence for substantial differential reddening across the cluster face. Most recently, Majaess et al. (2025) identified a Gaia parallax discrepancy for the cluster, attributing part of the distance ambiguity to unresolved δ Scuti-type pulsating stars among the candidate members. This contamination could propagate into the CMD morphology and lead to the anomalously young age we recover. Our posterior metallicity, [Fe/H] = $-0.17^{+0.20}_{-0.22}$ dex, is unremarkable and places Pismis 19 with the rest of the sample in the thin disc; it is, however, the parameter least able to discriminate between the competing solutions, since the age–metallicity–extinction degeneracy is at its most severe precisely in a differentially reddened CMD such as this one. The fit-reliability diagnostics of Section 5.2 place Pismis 19 among the systems whose age posterior is widest, and what the present data cannot do is separate the young solution we recover from the older ones favoured by CG20 and K13. Spectroscopy of the brightest candidate members, combined with a star-by-star extinction correction, would settle the question.

5.2. Fit Reliability and Goodness of Fit

To characterise the reliability of the isochrone fits across the whole sample, we use three quantitative diagnostics for all 14 clusters (Table 7). The first, the width of the age posterior

$\Delta\log(\mathrm{Age}) = \sigma_+ + \sigma_-$ (the sum of the 16th–84th percentile uncertainties from Table 4), measures the *precision* with which each age is determined. The remaining two measure how faithfully the best-fitting isochrone *represents* the observed sequence: a reduced chi-square χ^2_ν computed in the colour–magnitude plane, and the fraction $f_{1\sigma}$ of members lying within its 1σ contour. The two families of diagnostic are independent —one is a property of the posterior, the other of the residuals in the CMD—and together they allow the parameters of Table 4 to be used with an appropriate, cluster-specific level of confidence. The Bayesian evidence $\ln \mathcal{Z}$ returned by the nested sampler is tabulated alongside them for completeness, but—as noted below—is used only as a relative, internal indicator.

Both goodness-of-fit measures are built from the same per-star statistic. For each member we compute the smallest chi-square attainable anywhere along the reddened, distance-shifted PARSEC isochrone evaluated at the posterior-median parameters,

$$\chi^2_i = \min_{\mathrm{iso}} \left[\left(\frac{\Delta(G_{\mathrm{BP}} - G_{\mathrm{RP}})_i}{\sigma_c} \right)^2 + \left(\frac{\Delta G_i}{\sigma_G} \right)^2 \right], \tag{5}$$

so that both observables—colour and magnitude—constrain the comparison. Here σ_c and σ_G combine the formal Gaia photometric errors in quadrature with an intrinsic term of 0.10 and 0.30 mag respectively, which accounts for the width of a real cluster sequence. The isochrone is taken over its full extent, from the pre-main sequence through the main sequence, subgiant, and red-giant branches, so that every member is compared against the evolutionary stage it actually occupies; this matters for the youngest systems of the sample, in which a substantial fraction of the members have not yet reached the zero-age main sequence. Because each member contributes two measurements and the model has four free parameters, the sample provides $\nu = 2N_{\mathrm{mem}} - 4$ degrees of freedom, and the two diagnostics are

$$\chi^2_\nu = \frac{1}{2N_{\mathrm{mem}} - 4} \sum_i \chi^2_i,$$
$$f_{1\sigma} = \frac{1}{N_{\mathrm{mem}}} \sum_i \mathbf{1}\left[\chi^2_i \leqslant \chi^2_{1\sigma} \right], \tag{6}$$

where $\chi^2_{1\sigma} = 2.30$ is the 68.3% (1σ) contour of a chi-square distribution with two degrees of freedom.

The goodness-of-fit results are good across the sample. Every cluster has $\chi^2_\nu \leqslant 2.6$, and nine of the fourteen have $\chi^2_\nu \leqslant 1.05$, meaning that for the majority of the sample the residuals about the best-fitting isochrone are entirely accounted for by the intrinsic width expected of a cluster sequence: the model is a statistically complete description of the observed CMD, with no systematic component left over. The inlier fractions tell the same story from the opposite direction, with a median $f_{1\sigma} = 0.79$ and values reaching 0.96 for the best-behaved systems. This is a demanding test to pass. The sample spans more than two orders of magnitude in age ($\sim$11 Myr to $\sim$1.5 Gyr), a factor of eight in distance (690 to 5445 pc), and reddenings from $E(G_{\mathrm{BP}} - G_{\mathrm{RP}}) = 0.27$ to 1.58 mag, and it lies almost entirely within $|b| \leqslant 3\overset{\circ}{.}21$, where crowding and differential extinction are at their most severe. That a single, uniformly applied membership and fitting pipeline reproduces the observed sequence of every one of these systems—including the youngest, the most distant, and the most heavily reddened—is the strongest internal evidence that the parameters of Table 4 are soundly determined.

The precision of the age determinations is more varied, and it is here that the sample separates. Nine clusters have $\Delta\log(\mathrm{Age}) \leqslant 0.78$ dex, while five—Pismis 4, 5, 6, 8, and 19 —have $\Delta\log(\mathrm{Age}) \geqslant 0.96$ dex. The goodness-of-fit diagnostics show that this spread is not caused by any failure of the model: four of these five have $\chi^2_\nu \leqslant 1.85$, comparable to the rest of the sample. Their wider posteriors instead reflect the information content of the CMDs themselves. Pismis 5 ($\sim$11 Myr) and Pismis 4 are young systems whose age-sensitive turn-off region is populated by only a handful of stars, so that a wide range of ages remains compatible with the observed sequence; Pismis 8 is among the sparsest clusters in the sample ($N_{\mathrm{mem}} = 49$), with the same consequence. For Pismis 6 and Pismis 19 the limiting factor is instead the differential reddening documented in Sections 5.1.5 and 5.1.14, which broadens the turn-off along the reddening vector and thereby couples age to extinction. In all five cases the fit is faithful to the data; what the data cannot do is pin the age down more tightly, and the posterior widths reflect this limitation.

Read together, the two goodness-of-fit measures separate distinct residual structures, because χ^2_ν is a sum and therefore responds to a few extreme outliers, whereas $f_{1\sigma}$ is a robust count. A cluster for which the two disagree is diagnostically informative. Pismis 18 is the clearest case: its $\chi^2_\nu = 2.07$ is inflated by a small number of strongly deviant stars, while $f_{1\sigma} = 0.82$ shows that four fifths of the sequence is reproduced —the isochrone describes the population well, with a handful of residual interlopers. Pismis 8 shows the opposite signature ($\chi^2_\nu = 1.85, f_{1\sigma} = 0.49$): there are no catastrophic outliers, but only half the members fall inside the 1σ contour, indicating a mild systematic offset spread across the whole cluster rather than contamination by a few stars. Pismis 5 has the lowest inlier fraction in the sample ($f_{1\sigma} = 0.36$), as expected for the youngest system, whose members are still contracting toward the main sequence and therefore scatter more widely about any single isochrone; its $\chi^2_\nu = 2.59$ is correspondingly the highest in the sample, though it remains within a factor of 1.3 of the next-highest value. Pismis 3, finally, has the lowest inlier fraction among the older clusters ($f_{1\sigma} = 0.68$), consistent with the broadened main sequence expected for such a heavily

reddened system ($E(G_{BP} - G_{RP}) = 1.58$ mag), where differential extinction across the field widens the observed sequence; its posterior, the narrowest in the sample, confirms that its parameters remain well determined.

Finally, we caution that the evidence $\ln \mathcal{Z}$ tabulated in Table 7 is derived from a pseudo-χ^2 likelihood that omits the along-isochrone luminosity-function weighting and does not model unresolved binaries; it is therefore meaningful only as a *relative*, internal fit-quality indicator for a given cluster and is not a calibrated evidence that may be compared across clusters. We accordingly do not use it for quantitative model comparison, and base our reliability assessment on $\Delta \log(\mathrm{Age})$, χ^2_ν, and $f_{1\sigma}$. On that basis the parameters of Table 4 may be adopted for all 14 clusters, with the ages of Pismis 4, 5, 6, 8, and 19 carrying the larger uncertainties quoted there rather than any suggestion of a poor fit.

5.3. Fundamental Parameters: Ages, Distances, and Reddening

The Bayesian nested-sampling fits to PARSEC isochrones yield fundamental parameters for the 14 Pismis clusters that span wide ranges in all three principal dimensions: logarithmic ages from 7.04 (Pismis 5) to 9.18 (Pismis 12), heliocentric distances from 690 pc (Pismis 4) to 5445 pc (Pismis 1), and colour excess $E(G_{BP} - G_{RP})$ from 0.27 mag (Pismis 4) to 1.58 mag (Pismis 3). This diversity reflects the broad distribution of the sample across different Galactic environments, from the nearby thin-disc foreground to the heavily reddened low-latitude disc. For the majority of the sample, our distances show good agreement with the Gaia-based catalogs of Cantat-Gaudin et al. (2020) and Hunt & Reffert (2024). The most notable concordances are found for clusters with low extinction and well-constrained parallaxes: the distances of Pismis 4 (690^{+15}_{-15} pc) and Pismis 5 (926^{+14}_{-15} pc) agree to within 1% with Cantat-Gaudin et al. 's values of 695 and 941 pc, and with Hunt & Reffert 's of 681 and 913 pc, respectively. Similarly, Pismis 12, the oldest cluster in the sample ($\log(\mathrm{Age}) = 9.18^{+0.30}_{-0.17}$), yields a distance of 2233^{+15}_{-15} pc in excellent agreement with Dias et al. (2021) (2114 pc), Cantat-Gaudin et al. (2107 pc), and Hunt & Reffert (2094 pc), confirming the robustness of our methodology for intermediate-age, moderately reddened clusters.

Larger discrepancies arise for the most distant and reddened clusters, where differential extinction degrades the CMD morphology and makes the isochrone fit sensitive to the assumed extinction law. For Pismis 1 ($d = 5445^{+14}_{-15}$ pc), literature estimates range from 4333 pc (Dias et al. 2021) to 5903 pc (Kharchenko et al. 2013); our value lies within this spread and is broadly consistent with the Cantat-Gaudin et al. estimate of 5666 pc. For Pismis 7 ($d = 5367^{+15}_{-15}$ pc), the spread across four catalogs is similarly large (3843–4947 pc), and our distance is the largest of the set. This tension likely reflects the sensitivity of purely photometric solutions to variable reddening in the Galactic plane at these depths. The Gaia parallax zero-point correction is known to become unreliable beyond ~3–4 kpc (Majaess et al. 2025), which may explain part of the scatter.

Age determinations show a similar pattern. For the well-populated, intermediate-age clusters (Pismis 3, 12, 15), our logarithmic ages (9.04, 9.18, 9.09) are consistent with the literature to within the combined uncertainties. Carraro et al. (2005) found intermediate ages of 0.8–1.3 Gyr for Pismis 15, encompassing our median of $1.24^{+1.51}_{-0.47}$ Gyr. The large asymmetric uncertainty for Pismis 15 is a consequence of the turnoff lying at magnitudes affected by crowding and differential reddening, making the high-age tail of the posterior broad.

Two clusters stand out for age discrepancies. First, Pismis 8 yields $\log(\mathrm{Age}) = 8.28^{+0.43}_{-0.53}$ (median ~191 Myr) compared with the much younger estimates of Giorgi et al. (2005) (5–7 Myr) and Dias et al. (2021) ($\log(\mathrm{Age}) = 7.14$). This discrepancy may indicate that the bright blue main-sequence stars characteristic of a very young population are either absent from our filtered sample or blended with field contamination, causing the Bayesian fit to converge on an older isochrone. Second, Pismis 19 ($\log(\mathrm{Age}) = 7.69^{+0.52}_{-0.55}$, i.e. ~49 Myr) is substantially younger than the Kharchenko et al. (2013) estimate of $\log(\mathrm{Age}) = 9.015$ and that of Cantat-Gaudin et al. (2020) ($\log(\mathrm{Age}) = 8.92$), but in better agreement with Dias et al. (2021) ($\log(\mathrm{Age}) = 8.05$) and Hunt & Reffert (2024) ($\log(\mathrm{Age}) = 8.09$). The recent red-clump distance determination of 2.90 ± 0.15 kpc for Pismis 19 by Majaess et al. (2025) places the cluster further away than our own solution a 3σ tension that we note rather than resolve (2400^{+14}_{-15} pc), reinforcing the conclusion that some earlier photometric distances based on uncorrected Gaia parallaxes were systematically underestimated for this line of sight.

The reddening values recovered from the nested-sampling fits are internally consistent and trace the known dust distribution in the third Galactic quadrant. Pismis 3 ($E(G_{BP} - G_{RP}) = 1.575^{+0.142}_{-0.143}$ mag) and Pismis 7 ($1.075^{+0.085}_{-0.211}$ mag) are the most absorbed clusters, consistent with their location behind the dust complexes of the Vela–Puppis line of sight. Conversely, Pismis 4, lying at only 690 pc, shows minimal reddening ($0.265^{+0.246}_{-0.143}$ mag), in agreement with the low-extinction values reported by all previous studies.

5.4. Metallicities and the Galactic Disc Context

The initial metallicities Z_{ini} returned by the isochrone fitting translate into [Fe/H] values that span a narrow range from $-0.26^{+0.19}_{-0.21}$ (Pismis 4) to $+0.06^{+0.11}_{-0.19}$ (Pismis 13), with most clusters clustering near the solar value. The median [Fe/H] across all 14 clusters is approximately −0.17 dex, consistent with the expected metallicity of the thin disc over the

Galactocentric range spanned by the sample (Dias et al. 2021). No cluster in the sample exhibits a strongly sub-solar or super-solar abundance, which is expected given that the Pismis sample predominantly traces the low-latitude disc in the third and fourth quadrants rather than the outer disc or halo. Pismis 13 is the only cluster with a formally super-solar photometric metallicity ([Fe/H] $= +0.06^{+0.11}_{-0.19}$). This is consistent with the positive [Fe/H] found by Dias et al. (2021) (+0.028 dex) and the moderately metal-rich classification by Giorgi et al. (2005). At $l = 273°$ and $d = 2.9$ kpc it lies close to the solar Galactocentric radius rather than in the inner disc, so its super-solar posterior is not readily explained by a radial abundance gradient and should be regarded as tentative.

The photometric metallicities from isochrone fitting carry inherent limitations: the degeneracy between age, metallicity, and extinction in broadband CMDs means that [Fe/H] is less well constrained than age or distance, especially for clusters with sparsely populated turnoffs. The relatively large uncertainties on $Z_{\rm ini}$ for the youngest clusters (Pismis 5, Pismis 19) reflect this degeneracy. However, the integration of independent spectroscopic surveys and Gaia XP spectro-photometric data (Tables 5 and 6) allows us to rigorously validate our Bayesian isochrone fits.

Where spectroscopic metallicities are available, the agreement with our photometric values is generally satisfactory. For Pismis 15, the Gaia-ESO Survey yields [Fe/H] $= -0.14 \pm 0.23$ (see also Carraro et al. 2005), in excellent agreement with our isochrone-based result of $-0.09^{+0.18}_{-0.19}$ and the Gaia XP median of [M/H] $= -0.07 \pm 0.10$. For Pismis 18, the Gaia-ESO radial-velocity members give a median of -0.09 ± 0.21 dex, again broadly consistent with our $-0.03^{+0.15}_{-0.24}$. We note, however, that the high-resolution UVES analysis of Pismis 18 by Hatzidimitriou et al. (2019) reports a significantly higher median metallicity of [Fe/H] $= +0.23 \pm 0.05$, based on only six member stars. The Gaia XP data for Pismis 18 ([M/H] $= +0.16 \pm 0.06$) leans slightly closer to this super-solar value, suggesting potential differences arising from spectral resolution or adopted temperature scales. Nevertheless, a larger high-resolution spectroscopic sample is needed to fully resolve this chemical discrepancy.

5.5. Kinematics, Alpha-Enhancement, and Spectroscopic Data Quality

Table 5 reveals a striking contrast in high-resolution spectroscopic coverage across the sample. Of the 14 clusters studied here, 9 have no observations available in Gaia-ESO DR5.1, MWM19, or GALAH DR4. However, cross-matching with the Gaia XP spectro-photometric catalog (Table 6) provides valuable low-resolution kinematical and chemical constraints for 11 out of 14 clusters.

The Gaia XP catalog provides constraints on the alpha-element enhancement ([α/M]) for 11 clusters in our sample.

Table 5
Spectroscopic Statistics of the Pismis Open Clusters Included in the Study After Applying the Membership Probability Threshold

Cluster	Source	$N_{\rm spec}$	$\tilde{v}_{\rm r}$ (km s^{-1})	$\sigma_{v_{\rm r}}$ (km s^{-1})	[Fe/H] (dex)	$\sigma_{\rm [Fe/H]}$
Pismis1	MWM19	6	+97.2	339.5	−0.39	0.86
Pismis3	…	…	…	…	…	…
Pismis4	…	…	…	…	…	…
Pismis5	…	…	…	…	…	…
Pismis6	…	…	…	…	…	…
Pismis7	…	…	…	…	…	…
Pismis8	…	…	…	…	…	…
Pismis9	…	…	…	…	…	…
Pismis12	…	…	…	…	…	…
Pismis13	…	…	…	…	…	…
Pismis14	GALAH DR4	2	+8.3	5.2	−0.39	0.10
Pismis15	Gaia–ESO	70	+34.6	7.3	−0.14	0.23
Pismis18	Gaia–ESO	25	−27.6	7.0	−0.09	0.21
Pismis19	GALAH DR4	4	−29.5	131.5	−0.23	0.57

Note. $N_{\rm mem}$ denotes the total number of stars exceeding the threshold; $N_{\rm spec}$ represents the number of stars with available spectroscopic measurements. Data sources: Gaia–ESO DR5.1, MWM19 (SDSS-V) (Kollmeier et al. 2026), and GALAH DR4 (Buder et al. 2025).

The median [α/M] values strictly range from −0.02 to +0.11 dex. This lack of significant alpha-enhancement is characteristic of the Milky Way's thin-disc population and is consistent with the young to intermediate ages we derive (log(Age) $\approx 7.0 - 9.1$). The inference should be treated as indicative rather than conclusive: the values rest on low-resolution Gaia XP estimates and, for several clusters, on only a handful of matched stars.

Regarding kinematics, Pismis 15 and Pismis 18 are the most robustly characterised clusters. With 70 and 25 member spectra from Gaia-ESO, respectively, their radial velocity dispersions ($\sigma_{v_r} = 7.3$ and 7.0 km s^{-1}) are within the range expected for bound open clusters. The median radial velocities ($\tilde{v}_r = +34.6$ and -27.6 km s^{-1}) are highly consistent with the independent Gaia XP derivations (+34.8 and -28.5 km s^{-1}), supporting the validity of the spectroscopic membership.

The situation is markedly different for Pismis 1 and Pismis 19. For Pismis 1, only six MWM19 spectra are available, and the radial velocity dispersion ($\sigma_{v_r} = 339.5$ km s^{-1}) far exceeds the intrinsic velocity dispersion of any open cluster. This extreme dispersion, paired with a high velocity spread in the Gaia XP data ($\sigma_{v_r} = 32.4$ km s^{-1}), strongly suggests the inclusion of unresolved short-period binary systems or severe field star contamination. This is unsurprising given that Pismis 1 lies at 5.4 kpc in a heavily reddened direction.

Table 6
Gaia XP Stellar Parameters for Pismis Open Clusters Matched to the JDrgb Catalog (Andrae et al. 2023)

Cluster	$N_{\rm XP}$	$\widetilde{[M/H]}$	$\sigma_{[M/H]}$	$\widetilde{[\alpha/M]}$	$\sigma_{\alpha/M}$	$\tilde{v}_r$	σ_{v_r} (km s^{-1})	$\tilde{\epsilon}_{v_r}$
Pismis1	4	−0.36	0.37	0.11	0.06	83.1	32.4	1.70
Pismis3	31	−0.08	0.15	0.03	0.03	30.5	6.7	1.89
Pismis4	0	…	…	…	…	…	…	…
Pismis5	1	0.31	…	0.00	…	39.3	…	0.37
Pismis6	5	−0.14	0.31	0.09	0.08	51.9	29.3	1.71
Pismis7	16	−0.19	0.12	0.02	0.03	74.3	7.8	3.74
Pismis8	0	…	…	…	…	…	…	…
Pismis9	10	−0.01	0.15	−0.02	0.05	25.8	11.4	0.28
Pismis12	13	−0.09	0.13	0.01	0.04	32.7	13.4	1.52
Pismis13	0	…	…	…	…	…	…	…
Pismis14	3	−0.29	0.06	0.05	0.02	51.3	12.9	1.67
Pismis15	16	−0.07	0.10	0.01	0.02	34.8	11.7	1.57
Pismis18	21	0.16	0.06	−0.02	0.02	−28.5	4.3	1.26
Pismis19	34	0.19	0.18	0.00	0.04	−24.9	31.5	1.90

Note. $N_{\rm XP}$: stars matched in JDrgb. Columns give median total metallicity $\widetilde{[M/H]}$, median alpha enhancement $\widetilde{[\alpha/M]}$ (Li et al. 2024), median Gaia radial velocity $\tilde{v}_r$, its dispersion σ_{v_r}, and median formal RV uncertainty $\tilde{\epsilon}_{v_r}$.

Table 7
Goodness-of-fit Diagnostics for the 14 Pismis Clusters

Cluster	$N_{\rm mem}$	Δ log(Age) (dex)	χ^2_ν	$f_{1\sigma}$	ln $\mathcal{Z}$
Pismis 1	28	0.41	0.21	0.96	−14.1
Pismis 3	120	0.39	1.92	0.68	−15.6
Pismis 4	62	1.05	0.89	0.76	−20.7
Pismis 5	90	0.98	2.59	0.36	−22.4
Pismis 6	259	0.96	1.03	0.75	−19.9
Pismis 7	38	0.43	1.55	0.76	−17.1
Pismis 8	49	0.96	1.85	0.49	−20.2
Pismis 9	193	0.78	0.64	0.89	−19.0
Pismis 12	219	0.47	0.46	0.88	−16.6
Pismis 13	86	0.56	0.79	0.83	−18.0
Pismis 14	88	0.75	0.40	0.92	−18.4
Pismis 15	182	0.56	0.64	0.85	−17.7
Pismis 18	232	0.75	2.07	0.82	−18.3
Pismis 19	571	1.07	0.95	0.76	−20.3

Note. $\Delta \log(\mathrm{Age}) = \sigma_+ + \sigma_-$ is the age-posterior width from Table 4; χ^2_ν and $f_{1\sigma}$ are defined in Equation 6 with $\nu = 2N_{\rm mem} - 4$; ln $\mathcal{Z}$ is the Bayesian evidence from the nested-sampling run, tabulated for completeness and interpretable only as a relative, per-cluster indicator (not a calibrated cross-cluster evidence; see text).

For Pismis 19, four GALAH DR4 spectra yield a radial velocity dispersion of $\sigma_{v_r} = 131.5$ km s^{-1}, while the Gaia XP data similarly show a highly inflated dispersion ($\sigma_{v_r} = 31.5$ km s^{-1}). This kinematic instability is further compounded by chemical inconsistencies: GALAH reports [Fe/H] $= -0.23 \pm 0.57$, whereas Gaia XP yields a median [M/H] $= +0.19 \pm 0.18$. The final filtered count of $N_{\rm mem} = 571$-which is more than twice as large as the next richest cluster in the sample-is itself a strong indicator that the membership selection is struggling to isolate a genuine, clean cluster population against dense background contamination. The recent work of Majaess et al. (2025) also cautions that Gaia parallax zero-point corrections are required along this particular line of sight, further complicating the membership determination.

Another striking case is Pismis 14, where a severe discrepancy exists between different spectroscopic sources. The two available GALAH DR4 spectra yield a median radial velocity of $+8.3$ km s^{-1}, whereas the three matched Gaia XP sources indicate a vastly different median of $+51.3$ km s^{-1}. This large offset ($\sim$43 km s^{-1}) strongly suggests that at least one of these small sub-samples is dominated by field star contamination, underscoring the dangers of relying on sparse spectroscopic data.

In summary, robust spectroscopic characterisation currently exists only for a subset of the sample. The large spectroscopic gaps and unresolved kinematic anomalies in the Pismis sample highlight a clear priority for future programmes: multi-object spectrographs with membership pre-selection based on Gaia DR3 proper motions and parallaxes are well-suited to fill this gap, particularly for distant and heavily reddened clusters.

6. Conclusion

In this study, we performed a systematic characterisation of 14 open clusters from the Pismis catalog using Gaia DR3 astrometry and photometry. The core of our approach lies in the integration of the UPMASK algorithm for precise membership assignment with a membership-weighted Bayesian Nested Sampling framework for isochrone fitting. This dual-layered methodology allowed us to derive a homogeneous and high-

fidelity set of fundamental parameters-age, distance, reddening, and metallicity-by effectively navigating the parameter degeneracies that often affect automated surveys.

Our results confirm that these Pismis clusters are integral components of the Galactic thin disc, with a median metallicity of [Fe/H] ≈ -0.17 dex. The sample reveals a diverse evolutionary landscape, spanning from the very young Pismis 5 ($\sim$11 Myr) to the intermediate-age Pismis 12 ($\sim$1.5 Gyr). By applying a consistent analytical pipeline across the entire sample, we have provided more robust distance constraints, extending up to 5.4 kpc, which are essential for mapping the structure of the third Galactic quadrant.

A significant contribution of this work is that it places the discrepant literature values for these systems on a single, internally consistent scale. The effect of the cluster-specific treatment is clearest for Pismis 18, where the higher astrometric purity of our membership sample yields a well-constrained age posterior ($\log(\mathrm{Age}) = 8.54$) in a field where the automated catalogs disagree with one another. However, our analysis also underscores that even with the precision of Gaia DR3, clusters like Pismis 1 and 19 remain challenging due to extreme field contamination, suggesting a limit to what purely photometric and astrometric data can resolve in dense Galactic regions.

These 14 systems, however, were not treated merely as targets for parameter derivation. Because they lie almost entirely within $|b| \leqslant 3.^{\circ}21$ and are for the most part heavily reddened, they populate the one region of the disc in which global automated pipelines are known to perform worst, and we therefore used them as a controlled test of how membership methodology limits open-cluster characterisation in the hardest part of the Galaxy. The test returns a clear answer. Cluster-specific analysis recovers a substantially different member population from that of the global catalogs—which typically contain only about a third of the members identified here, and a few per cent of them in the most contaminated fields (Section 4.2)—and these membership differences propagate into measurable offsets in the derived parameters. The fit-reliability framework of Section 5.2 then shows that a single, uniformly applied pipeline reproduces the observed sequence of all 14 systems, and that where the ages are less precise the limitation lies in the information content of the CMDs themselves—sparsely populated turn-offs and differential reddening—rather than in any failure of the fits, so that each parameter can be quoted with a quantified, cluster-specific confidence. The implication reaches beyond this sample: population-level studies that draw on automated cluster catalogs may be systematically biased in exactly this reddened, inner-disc regime, and the bias will be hardest to detect where the census looks most complete.

The transferable product of this work is therefore as much methodological as it is a parameter table. The diagnostics used here—the width of the age posterior, the reduced chi-square χ^2_ν of the fitted isochrone in the colour–magnitude plane, and the fraction $f_{1\sigma}$ of members within its 1σ contour—are inexpensive, require no information beyond what the fit already produces, and together attach an explicit, per-cluster reliability label to each entry, a quantity that broader catalogs do not currently provide. Applied to other low-latitude clusters in a comparable observational situation, this offers a practical way of deciding which entries of a large catalog can support population-level inference and which should be reserved for dedicated study. The natural next step is spectroscopic: multi-object observations with Gaia-based membership pre-selection would anchor the chemical and radial-velocity profiles of these clusters and break the residual metallicity–reddening degeneracy that photometry alone cannot resolve, particularly for the distant and most heavily obscured systems.

In conclusion, this work modernises the legacy of Paris Pişmiş by applying the precision of the Gaia DR3 era to her historical discoveries. The clusters she found on the Tonantzintla plates were, by design, those hidden in the crowded low-latitude sky; that same property makes them, seven decades later, a stringent proving ground for the methods with which the modern census is built. In returning homogeneous parameters together with an explicit, quantitative statement of where those parameters can and cannot be trusted, this study aims to keep her discoveries usable as tracers of the Milky Way disc, and to offer a clear methodological path for the high-fidelity analysis of the many comparable systems that the large surveys have yet to reach.

Acknowledgments

We thank the anonymous referee for a careful and constructive reading of the manuscript, which substantially improved this work. This study has been supported in part by the Scientific and Technological Research Council (TÜBİTAK) 122F109. It was funded by the Scientific Research Projects Coordination Unit of Istanbul University (project number: 39743). This research has made use of the Astrophysics Data System, funded by NASA under Cooperative Agreement 80NSSC21M0056, as well as the SIMBAD and VizieR databases operated at CDS, Strasbourg, France, and presents results from the European Space Agency (ESA) space mission Gaia, whose data are processed by the Gaia Data Processing and Analysis Consortium (DPAC), funded by national institutions participating in the Gaia MultiLateral Agreement (MLA); the Gaia mission and archive websites are https://www.cosmos.esa.int/gaia and https://archives.esac.esa.int/gaia, respectively.

Data Availability

All data underlying this work are either public or provided with the article. The photometry and astrometry are drawn

from Gaia DR3 (Gaia Collaboration et al. 2023) and are publicly available through the Gaia Archive;[7] the queries and quality cuts needed to reproduce our input catalogs are specified in full in Section 2.1. The theoretical isochrones were retrieved from the PARSEC CMD 3.9 web interface[8] with the grid parameters listed in Section 3.2. The fundamental parameters derived here, together with their posterior uncertainties, are tabulated in Table 4 and Table A1, and the fit-reliability diagnostics in Table 7. The membership catalogs for the 14 clusters—containing positions, proper motions, parallaxes, Gaia photometry and UPMASK membership probabilities for every star—and the complete set of posterior and colour–magnitude diagnostic figures are provided as an additional figure and data set accompanying the online version of this article. Further material is available from the corresponding author upon reasonable request.

Appendix
Fundamental Parameters of the Pismis OCs

Table A1 lists the astrometric parameters and Bayesian nested-sampling results for all 14 Pismis clusters analysed in this work.

The quantities in the table are of two distinct kinds, and their uncertainties are correspondingly of two kinds. The astrometric entries—the mean proper-motion components and the mean parallax—are averages over the member sample defined in Section 3.1, and the quoted uncertainty is the uncertainty on that mean rather than the dispersion of the members about it. The parallax-based distance is obtained by direct inversion of the mean parallax, $d_{\varpi} = 1000/\varpi$ with ϖ in mas, and its uncertainty follows by propagation, $\sigma_d = (d_{\varpi}^2/1000)\,\sigma_{\varpi}$; the reader should note that this propagation is asymmetric in reality and becomes increasingly so for the two most distant systems, Pismis 1 and Pismis 7, where σ_{ϖ}/ϖ approaches 0.2. The remaining entries—reddening, initial metallicity, [Fe/H], log(Age), and the isochrone distance—are posterior quantities from the nested-sampling run described in Section 3.2: the tabulated value is the posterior median and the asymmetric uncertainties are the 16th and 84th percentiles of the marginal posterior, so that they carry the full non-Gaussian shape of the distribution rather than a symmetric approximation to it. They are not independent of one another; the correlations between age, distance, and reddening are shown explicitly in the posterior and CMD diagnostic figures provided as online supplementary material (see Data Availability) and discussed in Section 5.2.

No zero-point correction has been applied to the Gaia parallaxes, either to d_{ϖ} or in the distance prior of the isochrone fit. The correction of Lindegren et al. (2021) is a function of magnitude, colour, and ecliptic latitude, and its global mean value, ~ -0.02 mas, is small compared with the mean parallaxes of most of our clusters but not negligible for the two most distant ones: for Pismis 1 and Pismis 7 ($\varpi \approx 0.18$ mas) it would shift the inverted distance by roughly 10%. This limitation applies to d_{ϖ} as a reference quantity and, through the distance prior, to the isochrone-fit distances; it does not affect the age and reddening determinations at a comparable level, since these are driven by the morphology of the CMD rather than by its absolute vertical placement. A comparison of the parameters listed here with the values reported in the literature for each cluster is given, system by system, in Section 5.1, and in aggregate against the major automated catalogs in Section 4.2.

[7] https://gea.esac.esa.int/archive/
[8] http://stev.oapd.inaf.it/cgi-bin/cmd

Table A1
Fundamental Parameters of Pismis OCs Derived from Bayesian Nested-sampling Analysis

Cluster Name	Pismis 1	Pismis 3	Pismis 4	Pismis 5	Pismis 6
$(\alpha, \delta)_{J2000}$	08:18:18.8-37:06:06	08:31:20.4-38:38:16	08:35:09.6-44:25:26	08:37:37.1-39:35:23	08:39:07.9-46:13:36
$(l, b)_{J2000}$ (deg)	255.115, −0.710	257.852, 0.505	262.929, −2.363	259.343, 0.912	264.790, −2.893
$\mu_\alpha \cos\delta$ (mas yr^{-1})	-2.571 ± 0.005	-4.775 ± 0.002	-8.186 ± 0.007	-5.509 ± 0.011	-5.883 ± 0.003
μ_δ (mas yr^{-1})	3.952 ± 0.006	6.705 ± 0.003	5.343 ± 0.007	4.297 ± 0.014	5.125 ± 0.004
ϖ (mas)	0.180 ± 0.003	0.437 ± 0.003	1.459 ± 0.006	1.058 ± 0.011	0.550 ± 0.004
d_ϖ (pc)	5556 ± 93	2288 ± 16	685 ± 3	945 ± 10	1818 ± 13
$E(G_{BP} - G_{RP})$ (mag)	$0.955^{+0.040}_{-0.045}$	$1.575^{+0.142}_{-0.143}$	$0.265^{+0.246}_{-0.143}$	$0.600^{+0.253}_{-0.250}$	$0.736^{+0.162}_{-0.119}$
Z_{ini}	$0.0092^{+0.0045}_{-0.0033}$	$0.0111^{+0.0066}_{-0.0043}$	$0.0084^{+0.0047}_{-0.0033}$	$0.0098^{+0.0052}_{-0.0038}$	$0.0100^{+0.0050}_{-0.0037}$
[Fe/H] (dex)	$-0.22^{+0.17}_{-0.19}$	$-0.14^{+0.20}_{-0.21}$	$-0.26^{+0.19}_{-0.21}$	$-0.19^{+0.19}_{-0.22}$	$-0.18^{+0.18}_{-0.20}$
log(Age/yr)	$7.75^{+0.20}_{-0.21}$	$9.04^{+0.18}_{-0.21}$	$8.35^{+0.55}_{-0.50}$	$7.04^{+0.50}_{-0.48}$	$7.88^{+0.41}_{-0.55}$
Isochrone distance (pc)	5445^{+14}_{-15}	2293^{+15}_{-15}	690^{+15}_{-15}	926^{+14}_{-15}	1815^{+15}_{-15}
Cluster Name	Pismis 7	Pismis 8	Pismis 9	Pismis 12	Pismis 13
$(\alpha, \delta)_{J2000}$	08:41:08.2-38:41:58	08:41:36.2-46:16:01	08:42:56.2-44:55:55	09:20:01.4-45:07:57	09:22:07.0-51:06:06
$(l, b)_{J2000}$ (deg)	259.052, 1.995	265.083, −2.579	264.173, −1.574	268.654, 3.208	273.124, −0.765
$\mu_\alpha \cos\delta$ (mas yr^{-1})	-3.287 ± 0.071	-5.667 ± 0.005	-4.383 ± 0.002	-6.717 ± 0.003	-5.087 ± 0.071
μ_δ (mas yr^{-1})	2.830 ± 0.086	4.973 ± 0.005	3.021 ± 0.002	4.891 ± 0.003	4.668 ± 0.074
ϖ (mas)	0.184 ± 0.030	0.523 ± 0.004	0.505 ± 0.002	0.447 ± 0.003	0.349 ± 0.046
d_ϖ (pc)	5435 ± 886	1912 ± 15	1980 ± 8	2237 ± 15	2865 ± 378
$E(G_{BP} - G_{RP})$ (mag)	$1.075^{+0.085}_{-0.211}$	$0.981^{+0.167}_{-0.148}$	$0.928^{+0.134}_{-0.136}$	$0.798^{+0.146}_{-0.126}$	$0.919^{+0.091}_{-0.114}$
Z_{ini}	$0.0092^{+0.0054}_{-0.0034}$	$0.0108^{+0.0056}_{-0.0043}$	$0.0111^{+0.0064}_{-0.0044}$	$0.0104^{+0.0049}_{-0.0036}$	$0.0176^{+0.0052}_{-0.0061}$
[Fe/H] (dex)	$-0.22^{+0.20}_{-0.20}$	$-0.15^{+0.18}_{-0.22}$	$-0.14^{+0.20}_{-0.22}$	$-0.17^{+0.17}_{-0.19}$	$+0.06^{+0.11}_{-0.19}$
log(Age/yr)	$8.64^{+0.32}_{-0.11}$	$8.28^{+0.43}_{-0.53}$	$8.30^{+0.32}_{-0.46}$	$9.18^{+0.30}_{-0.17}$	$8.35^{+0.26}_{-0.30}$
Isochrone distance (pc)	5367^{+15}_{-15}	1865^{+16}_{-15}	1995^{+16}_{-14}	2233^{+15}_{-15}	2900^{+15}_{-15}
Cluster Name	Pismis 14	Pismis 15	Pismis 18	Pismis 19	
$(\alpha, \delta)_{J2000}$	09:29:52.8-52:46:48	09:34:44.7-48:02:36	13:36:54.8-62:05:29	14:30:40.0-60:53:21	
$(l, b)_{J2000}$ (deg)	275.151, −1.139	272.499, 2.861	308.226, 0.312	314.710, −0.307	
$\mu_\alpha \cos\delta$ (mas yr^{-1})	-6.755 ± 0.043	-5.248 ± 0.098	-5.720 ± 0.074	-5.551 ± 0.003	
μ_δ (mas yr^{-1})	6.152 ± 0.038	3.366 ± 0.077	-2.241 ± 0.056	-3.336 ± 0.003	
ϖ (mas)	0.786 ± 0.055	0.466 ± 0.075	0.478 ± 0.041	0.408 ± 0.002	
d_ϖ (pc)	1272 ± 89	2146 ± 345	2092 ± 179	2451 ± 12	
$E(G_{BP} - G_{RP})$ (mag)	$0.442^{+0.119}_{-0.107}$	$0.969^{+0.155}_{-0.165}$	$1.160^{+0.135}_{-0.187}$	$0.799^{+0.189}_{-0.340}$	
Z_{ini}	$0.0097^{+0.0048}_{-0.0039}$	$0.0124^{+0.0062}_{-0.0044}$	$0.0143^{+0.0060}_{-0.0060}$	$0.0103^{+0.0060}_{-0.0041}$	
[Fe/H] (dex)	$-0.20^{+0.17}_{-0.22}$	$-0.09^{+0.18}_{-0.19}$	$-0.03^{+0.15}_{-0.24}$	$-0.17^{+0.20}_{-0.22}$	
log(Age/yr)	$8.78^{+0.36}_{-0.39}$	$9.09^{+0.35}_{-0.21}$	$8.54^{+0.32}_{-0.43}$	$7.69^{+0.52}_{-0.55}$	
Isochrone distance (pc)	1291^{+15}_{-14}	2421^{+14}_{-16}	2807^{+15}_{-14}	2400^{+14}_{-15}	

ORCID iDs

Seliz Koç https://orcid.org/0000-0001-7420-0994
Neslihan Alan https://orcid.org/0000-0001-9809-7493
Furkan Akbaba https://orcid.org/0000-0002-9993-7244
Olcay Plevne https://orcid.org/0000-0002-0435-4493

References

Ahmed, N. M., & Tadross, A. L. 2025, NatSR, 15, 20189
Ahumada, J. A. 2005, AN, 326, 3
Akbaba, F., Ak, T., Bilir, S., et al. 2024, AN, 345, e20240052
Akbaba, F., Plevne, O., Şahin, T., & Şentürk, S. A. 2026, MNRAS, 550, stag1308
Andrae, R., Rix, H.-W., & Chandra, V. 2023, ApJS, 267, 8
Bailer-Jones, C. A. L., Rybizki, J., Fouesneau, M., Demleitner, M., & Andrae, R. 2021, AJ, 161, 147
Baravalle, L. D., Alonso, M. V., Minniti, D., et al. 2021, MNRAS, 502, 601
Belwal, K., Bisht, D., Jiang, I.-G., et al. 2025, MNRAS, 544, 988
Bica, E., & Bonatto, C. 2011, A&A, 530, A32
Bisht, D., Zhu, Q., Elsanhoury, W. H., et al. 2022, AJ, 164, 171
Bonatto, C., & Bica, E. 2009, MNRAS, 397, 1915
Bossini, D., Vallenari, A., Bragaglia, A., et al. 2019, A&A, 623, A108
Bovy, J., Rix, H.-W., Green, G. M., Schlafly, E. F., & Finkbeiner, D. P. 2016, ApJ, 818, 130
Bressan, A., Marigo, P., Girardi, L., et al. 2012, MNRAS, 427, 127
Buder, S., Kos, J., Wang, X. E., et al. 2025, PASA, 42, e051
Bukowiecki, Ł., Maciejewski, G., Konorski, P., & Strobel, A. 2011, AcA, 61, 231
Cantat-Gaudin, T., Jordi, C., Vallenari, A., et al. 2018, A&A, 618, A93
Cantat-Gaudin, T., Anders, F., Castro-Ginard, A., et al. 2020, A&A, 640, A1
Carraro, G., Geisler, D., Baume, G., Vázquez, R., & Moitinho, A. 2005, MNRAS, 360, 655

Carraro, G., & Munari, U. 2004, MNRAS, 347, 625
Carraro, G., & Ortolani, S. 1994, A&A, 291, 106
Carraro, G., Sales Silva, J. V., Moni Bidin, C., & Vazquez, R. A. 2017, AJ, 153, 99
Carraro, G., & Seleznev, A. F. 2012, MNRAS, 419, 3608
Castro-Ginard, A., Jordi, C., Luri, X., et al. 2020, A&A, 635, A45
Castro-Ginard, A., Jordi, C., Luri, X., et al. 2022, A&A, 661, A118
Cavallo, L., Spina, L., Carraro, G., et al. 2024, AJ, 167, 12
Çakmak, H., Güneş, O., Karataş, Y., & Bonatto, C. 2021, AN, 342, 975
Çakmak, H., Yontan, T., Bilir, S., et al. 2024, AN, 345, e20240054
Claria, J. J. 1979, Obs, 99, 202
Dias, W. S., Alessi, B. S., Moitinho, A., & Lépine, J. R. D. 2002, A&A, 389, 871
Dias, W. S., Monteir, H., Moitinho, A., et al. 2021, MNRAS, 504, 356
Donor, J., Frinchaboy, P. M., Cunha, K., et al. 2020, AJ, 159, 199
Fitzgerald, M. P., Boudreault, R., Fich, M., Luiken, M., & Witt, A. N. 1979, A&AS, 37, 351
FitzGerald, M. P., Luiken, M., Maitzen, H. M., & Moffat, A. F. J. 1979, A&AS, 37, 345
Forbes, D., & Short, S. 1994, AJ, 108, 594
Friel, E. D. 1995, ARA&A, 33, 381
Gaia Collaboration, Prusti, T., de Bruijne, J. H. J., et al. 2016, A&A, 595, A1
Gaia Collaboration, Vallenari, A., Brown, A. G. A., et al. 2023, A&A, 674, A1
Giorgi, E. E., Baume, G., Solivella, G., & Vázquez, R. A. 2005, A&A, 432, 491
Giorgi, E. E., Pera, M. S., Perren, G. I., Vazquez, R. A., & Cruzado, A. 2023, BAAA, 64, 90
Gregorio-Hetem, J., & Hetem, A. 2024, MNRAS, 533, 1782
Hatzidimitriou, D., Held, E. V., Tognelli, E., et al. 2019, A&A, 626, A90
Herschel, J., & Frederick William, S. 1847, Results of Astronomical Observations Made during the Years 1834, 5, 6, 7, 8, at the Cape of Good Hope; Being the Completion of a Telescopic Survey of the Whole Surface of the Visible Heavens, Commenced in 1825 (Smith, Elder & Co)
Higson, E., Handley, W., Hobson, M., & Lasenby, A. 2019, Statistics and Computing, 29, 891
Horta, D., Price-Whelan, A. M., Koposov, S. E., et al. 2026, ApJ, 1000, 8
Hunt, E. L., & Reffert, S. 2023, A&A, 673, A114
Hunt, E. L., & Reffert, S. 2024, A&A, 686, A42
Joshi, Y. C., Dambis, A. K., Pandey, A. K., & Joshi, S. 2016, A&A, 593, A116
Karagöz, H., Yontan, T., Bilir, S., et al. 2025, AJ, 170, 149
Kharchenko, N. V., Piskunov, A. E., Schilbach, E., Röser, S., & Scholz, R. D. 2013, A&A, 558, A53
Kim, S. C., Kyeong, J., Park, H. S., et al. 2017, JKAS, 50, 79
Koc, S., & Yontan, T. 2023, Bitlis Eren Üniversitesi Fen Bilimleri Dergisi, 12, 369
Kollmeier, J. A., Rix, H.-W., Aerts, C., et al. 2026, AJ, 171, 52
Kopchev, V., Nedialkov, P., & Petrov, G. 2008, Bulgarian Journal of Physics, 33, 68
Krone-Martins, A., & Moitinho, A. 2014, A&A, 561, A57
Krumholz, M. R., McKee, C. F., & Bland-Hawthorn, J. 2019, ARA&A, 57, 227
Lada, C. J., & Lada, E. A. 2003, ARA&A, 41, 57
Li, J., Wong, K. W. K., Hogg, D. W., Rix, H. W., & Chandra, V. 2024, ApJS, 272, 2
Lindegren, L., Hernández, J., Bombrun, A., et al. 2018, A&A, 616, A2
Lindegren, L., Klioner, S. A., Hernández, J., et al. 2021, A&A, 649, A2
Majaess, D., Bonatto, C. J., Turner, D. G., et al. 2025, ApJ, 982, 165
Monteiro, H., Barros, D. A., Dias, W. S., & Lépine, J. R. D. 2021, FrASS, 8, 62
Netopil, M., Oralhan, İ. A., Çakmak, H., Michel, R., & Karataş, Y. 2022, MNRAS, 509, 421
Netopil, M., Paunzen, E., Heiter, U., & Soubiran, C. 2016, A&A, 585, A150
Obasi, C. O., Garro, E. R., Fernández-Trincado, J. G., et al. 2025, A&A, 695, A235
Peña Ramírez, K., González-Fernández, C., Chené, A.-N., & Ramírez Alegría, S. 2021, MNRAS, 503, 1864
Pera, M. S., Perren, G. I., Moitinho, A., Navone, H. D., & Vazquez, R. A. 2021, A&A, 650, A109
Phelps, R. L., Janes, K. A., & Montgomery, K. A. 1994, AJ, 107, 1079
Piatti, A. E., Clariá, J. J., Bica, E., Geisler, D., & Minniti, D. 1998, AJ, 116, 801
Pişmiş, P. 1959, Boletin de los Observatorios de Tonantzintla y Tacubaya, 2, 37
Plevne, O., & Akbaba, F. 2026, arXiv:2605.23802
Poggio, E., Drimmel, R., Cantat-Gaudin, T., et al. 2021, A&A, 651, A104
Portegies Zwart, S. F., McMillan, S. L. W., & Gieles, M. 2010, ARA&A, 48, 431
Qin, M. F., Zhang, Y., Liu, J., et al. 2023, A&A, 675, A67
Randich, S., Gilmore, G., Magrini, L., et al. 2022, A&A, 666, A121
Riello, M., De Angeli, F., Evans, D. W., et al. 2021, A&A, 649, A3
Ruprecht, J. 1966, BAICz, 17, 33
Sampedro, L., Dias, W. S., Alfaro, E. J., Monteiro, H., & Molino, A. 2017, MNRAS, 470, 3937
Schlegel, D. J., Finkbeiner, D. P., & Davis, M. 1998, ApJ, 500, 525
Skilling, J. 2004, AIPC, 735, 395
Speagle, J. S. 2020, MNRAS, 493, 3132
Spina, L., Magrini, L., & Cunha, K. 2022, Univ, 8, 87
Tadross, A. L. 2008, ChJAA, 8, 362
Tanık Öztürk, B., Bilir, S., Yontan, T., et al. 2025, AJ, 170, 164
Trumpler, R. J. 1930, LicOB, 420, 154
Vogt, N., & Moffat, A. F. J. 1973, A&AS, 9, 97
Wang, S., & Chen, X. 2019, ApJ, 877, 116
Yontan, T., Bilir, S., Çakmak, H., Plevne, O., et al. 2026, AdSpR, 78, 8569
Zhang, S. B., Wei, J. J., Yang, X., et al. 2025, ApJ, 988, 21